

# OT-ALD: Aligning Latent Distributions with Optimal Transport for Accelerated Image-to-Image Translation

Zhanpeng Wang<sup>1</sup>, Shuting Cao<sup>1</sup>, Yuhang Lu<sup>1</sup>, Yuhan Li<sup>1</sup>, Na Lei<sup>1\*</sup>, Zhongxuan Luo<sup>1</sup>

<sup>1</sup>Dalian University of Technology, Dalian, Liaoning, China

## Abstract

The Dual Diffusion Implicit Bridge (DDIB) is an emerging image-to-image (I2I) translation method that preserves cycle consistency while achieving strong flexibility. It links two independently trained diffusion models (DMs) in the source and target domains by first adding noise to a source image to obtain a latent code, then denoising it in the target domain to generate the translated image. However, this method faces two key challenges: (1) low translation efficiency, and (2) translation trajectory deviations caused by mismatched latent distributions. To address these issues, we propose a novel I2I translation framework, OT-ALD, grounded in optimal transport (OT) theory, which retains the strengths of DDIB-based approach. Specifically, we compute an OT map from the latent distribution of the source domain to that of the target domain, and use the mapped distribution as the starting point for the reverse diffusion process in the target domain. Our error analysis confirms that OT-ALD eliminates latent distribution mismatches. Moreover, OT-ALD effectively balances faster image translation with improved image quality. Experiments on four translation tasks across three high-resolution datasets show that OT-ALD improves sampling efficiency by 20.29% and reduces the FID score by 2.6 on average compared to the top-performing baseline models.

## Introduction

Image-to-image (I2I) translation is a fundamental task in computer vision that involves transforming an image from a source domain to a target domain while preserving its structural and semantic integrity. This technique has broad applications, including image restoration (Liang et al. 2021; Zamir et al. 2022), style transfer (Azadi et al. 2018; Gatys, Ecker, and Bethge 2016), and image synthesis (Rombach et al. 2022; Odena, Olah, and Shlens 2017), among others. The rapid advancement of deep generative models has led to significant progress in I2I translation, giving rise to numerous state-of-the-art methods. In particular, generative adversarial networks (GANs) (Zhu et al. 2017; Isola et al. 2017; Yi et al. 2017; Kim et al. 2017; Fu et al. 2019; Park et al. 2020; Benaim and Wolf 2017) have played a pivotal role in early developments. More recently, diffusion models (DMs) (Sasaki, Willcocks, and Breckon 2021; Su et al. 2022; Zhao

et al. 2022; Saharia et al. 2022a; Wang et al. 2022a,b; Li et al. 2023a; Kwon and Ye 2022; Parmar et al. 2023; Meng et al. 2021) have gained prominence and become a major focus in contemporary research due to their ability to produce high-quality, diverse outputs.

The contraction property of DMs (Carrillo, McCann, and Villani 2006; Khrulkov et al. 2022; Franzese et al. 2023), as illustrated in Fig. 1(b), significantly contributes to their rapid adoption in I2I translation. The core mechanism of DMs involves systematically corrupting a real image by progressively adding noise until it becomes pure Gaussian noise (Ho, Jain, and Abbeel 2020). Subsequently, the model learns to reconstruct the original image from noise through score matching (Song et al. 2020). This reconstruction is facilitated via a reverse process that incrementally removes noise, guiding the image from a random state back to the real data distribution. Mathematically, these forward and reverse processes are described by a pair of stochastic differential equations (SDEs) (Song et al. 2020; Anderson 1982). Currently, diffusion-based I2I translation methods can be roughly categorized into two types: (1) Utilizing the source image to guide the generation trajectory of the target image (Zhao et al. 2022; Choi et al. 2021; Meng et al. 2021; Sun et al. 2023; Li and Ma 2023; Lugmayr et al. 2022; Kim, Kwon, and Ye 2022; Tumanyan et al. 2023; Seo et al. 2023; Yang et al. 2023; Zhang et al. 2023b), ensuring that the output evolves toward the desired target. However, this approach relies on joint training on both the source and target domains, necessitating simultaneous access to both datasets. This requirement limits data separation, undermines privacy protection, and reduces the overall flexibility. (2) Interconnecting two independently trained DMs in the source and target domains (Su et al. 2022; Yu et al. 2023; Zhang et al. 2023a; Popov et al. 2023; Zhang et al. 2024; Bourou et al. 2024; Hur et al. 2024; Yin et al. 2024; Mancusi et al. 2024), a technique referred to as the Dual Diffusion Implicit Bridges (DDIB)-based method. Firstly, the source domain DM adds noise to the source image, transforming it into a latent code. The target domain DM then progressively denoises the latent code to generate the target image. This method enables I2I translation while ensuring privacy protection and high flexibility.

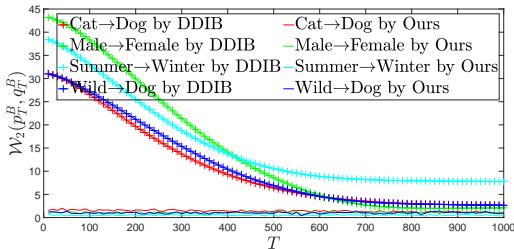
The DDIB-based method is not without its limitations. First, employing two DMs leads to increased inference time

\*Corresponding author. Email: nalei@dlut.edu.cn  
Copyright © 2026, Association for the Advancement of Artificial Intelligence (www.aaai.org). All rights reserved.

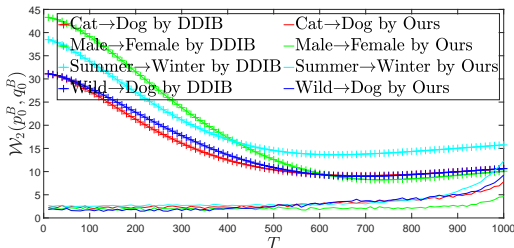
(Su et al. 2022). Second, in practical applications, DMs must terminate after a finite number of time steps, meaning the termination distributions (latent code distributions) of the source and target domain DMs do not perfectly align with the standard Gaussian distribution. This misalignment introduces a theoretical gap, which has been shown to cause deviations in the image translation trajectory within the target domain. As a result, even with high-precision score matching training for both DMs, the translated images may fail to fully conform to the intended target distribution (see Theorem 1). Furthermore, the cycle consistency of the DDIB-based method may also be compromised.



(a) The translation effect of the proposed model on multiple high-resolution image tasks



(b) Wasserstein difference in latent distributions



(c) Wasserstein difference in target distributions

Fig 1: (a) Top-row images are sources and bottom-row images are corresponding outputs generated by our model. (b) Contraction property of DMs. For initial distributions from different domains, DMs can exponentially shrink Wasserstein distance between their latent distributions through progressive noise injection.  $T$  is the number of diffusion steps, and  $q_T^B$  is initial distribution for the reverse process of  $DM^B$ . In DDIB-based methods,  $q_T^B = p_T^A$ , while OT-ALD aligns latent distributions via OT map  $M_{ot,T}^{A \rightarrow B}$  to ensure  $q_T^B = M_{ot,T}^{A \rightarrow B}(p_T^A)$ . (c) Latent alignment impacts how closely the translated distribution approximates the ground truth (Theorem 1). DDIB requires longer diffusion to compensate for misalignment, reducing efficiency. OT-ALD is less sensitive to  $T$ , but empirically, too few steps harm image quality/diversity, and too many accumulate errors.

To address the abovementioned issues, we propose to eliminate this gap by aligning the latent code distribution using an optimal transport (OT) map (see Theorem 2). The main contributions of this paper are summarized as follows:

- We demonstrate that existing DDIB-based I2I translation methods suffer from a theoretical gap caused by a mismatch between latent distributions. As a result, even with perfectly accurate score matching, the translation trajectory may still deviate from the intended target distribution.
- Building on OT, we propose a novel I2I translation framework, OT-ALD, which theoretically aligns the latent distributions. Our theoretical analysis and experimental results show that OT-ALD inherits cycle consistency and strong flexibility of the DDIB-based approach.
- OT-ALD can strike a balance between accelerating I2I translation and enhancing the quality of image generation. Experiments on four tasks across three high-resolution datasets show that compared with the best baseline model, OT-ALD achieves an average 20.29% improvement in sampling efficiency and 2.6 reduction in FID.

## Preliminaries and related works

In this section, we first overview the background on image synthesis using DMs. Next, we introduce the theoretical framework of OT. Finally, we review the relevant literature related to this study.

### Image synthesis through the DMs

The DMs include forward and reverse processes. Given the drift coefficient  $\mathbf{f}(\mathbf{x}, t) : \mathbb{R}^n \times [0, T] \rightarrow \mathbb{R}^n$  and the diffusion term  $g(t) : [0, T] \rightarrow \mathbb{R}_{>0}$ , the internal mechanism of the forward process can be elucidated by the following SDE (Song et al. 2020)

$$d\mathbf{x} = \mathbf{f}(\mathbf{x}, t) dt + g(t) d\mathbf{W}_t, \mathbf{x}(0) \sim p_0(\mathbf{x}), \quad (1)$$

where  $p_0(\mathbf{x})$  is the image distribution and  $\mathbf{W}_t$  is the  $n$ -dimensional standard Wiener process. The marginal distribution of the solution to (1),  $p_t(\mathbf{x})$ , satisfies the Fokker-Planck equation (FPE) (Risken and Risken 1996)

$$\frac{\partial p_t(\mathbf{x})}{\partial t} + \nabla \cdot (\mathbf{f}(\mathbf{x}, t) p_t(\mathbf{x})) - \frac{g(t)^2}{2} \Delta p_t(\mathbf{x}) = 0. \quad (2)$$

According to (2), there exists a deterministic process, referred to as the probability flow ordinary differential equation (PF-ODE) (Song et al. 2020), which shares the same marginal probability density  $p_t$  as (1)

$$d\mathbf{x} = (\mathbf{f}(\mathbf{x}, t) - \frac{g(t)^2}{2} \nabla \log p_t(\mathbf{x})) dt, \mathbf{x}(0) \sim p_0(\mathbf{x}).$$

Similarly, the reverse process can be expressed as reverse-time SDE (Anderson 1982) with  $q_T$  as the initial condition

$$d\mathbf{x} = (\mathbf{f}(\mathbf{x}, t) - g(t)^2 \nabla \log p_t(\mathbf{x})) dt + g(t) d\bar{\mathbf{W}}_t, \quad (3)$$

where  $\mathbf{x}(T) \sim q_T(\mathbf{x})$  and  $\bar{\mathbf{W}}_t$  is the  $n$ -dimensional standard Wiener process with backward time. In practice,  $\nabla \log p_t(\mathbf{x})$  is usually approximated by a score network

$\mathbf{S}_\theta(\mathbf{x}, t) : \mathbb{R}^n \times [0, T] \rightarrow \mathbb{R}^n$  with the weighted mean square error (MSE) loss function (Song et al. 2021)

$$\mathcal{J}_{SM}(\theta, \phi, T) := \frac{1}{2} \int_0^T \phi(t) \mathbb{E}_{p_t} [\|\mathbf{S}_\theta(\mathbf{x}, t) - \nabla \log p_t(\mathbf{x})\|_2^2] dt,$$

here  $\phi(t) : [0, T] \rightarrow \mathbb{R}_{>0}$  is a positive weighting function. By replacing  $\nabla \log p_t(\mathbf{x})$  with  $\mathbf{S}_\theta(\mathbf{x}, t)$  in the reverse process, we get an approximate reverse-time SDE and FPE. Ultimately, the approximate image distribution  $q_0$  is obtained from  $q_T$ . The solution of DMs can be formalized as

$$\begin{aligned} & \text{Solver}_\eta(\mathbf{x}_{t_0}, \mathbf{S}_\theta, t_0, t_1) \\ &= \mathbf{x}_{t_0} + \int_{t_0}^{t_1} \mathbf{v}_\theta(\mathbf{x}, t) dt + \eta \int_{t_0}^{t_1} g(t) d\mathbf{W}_t, \end{aligned} \quad (4)$$

where  $\mathbf{v}_\theta(\mathbf{x}, t) = \mathbf{f}(\mathbf{x}, t) - \frac{1}{2}(1 - \eta^2)g(t)^2 \mathbf{S}_\theta(\mathbf{x}, t)$  and  $\eta \in [0, 1]$  denotes noise scaling factor.

### Optimal transport theory

We begin by introducing the classical geometric variational approach to semi-discrete OT. As the number of target samples increases, the discrete solution progressively converges to its continuous counterpart. Suppose the source measure  $\mu$  is defined on a convex domain  $\Omega \subset \mathbb{R}^n$ , and the target domain is a discrete set  $\mathcal{Y} = \{\mathbf{y}_i\}_{i \in \mathcal{I}} \subset \mathbb{R}^n$ . The target measure is a Dirac measure  $\nu = \sum_{i \in \mathcal{I}} \nu_i \delta(\mathbf{y} - \mathbf{y}_i)$ , with the total mass matched as  $\mu(\Omega) = \sum_{i \in \mathcal{I}} \nu_i$ . Under a transport map  $M : \Omega \rightarrow \mathcal{Y}$ , the domain  $\Omega$  is partitioned into cells  $W_i$  such that each point  $\mathbf{x} \in W_i$  is mapped to  $\mathbf{y}_i$ , i.e.,  $M(\mathbf{x}) = \mathbf{y}_i$ . The map  $M$  is measure-preserving (denoted  $M_{\#}\mu = \nu$ ) if each cell satisfies  $\mu(W_i) = \nu_i$ . Let  $c : \Omega \times \mathcal{Y} \rightarrow \mathbb{R}$  be the cost function, where  $c(\mathbf{x}, \mathbf{y})$  denotes the cost of transporting unit mass from  $\mathbf{x}$  to  $\mathbf{y}$ . The total transport cost of the map  $M$  is given by

$$\int_{\Omega} c(\mathbf{x}, M(\mathbf{x})) d\mu(\mathbf{x}) = \sum_{i \in \mathcal{I}} \int_{W_i} c(\mathbf{x}, \mathbf{y}_i) d\mu(\mathbf{x}). \quad (5)$$

The OT map  $M_{ot}$  is a measure-preserving map that minimizes the total cost in (5),

$$M_{ot} := \arg \min_{M_{\#}\mu = \nu} \int_{\Omega} c(\mathbf{x}, M(\mathbf{x})) d\mu(\mathbf{x}). \quad (6)$$

Specifically, when the cost function is  $c(\mathbf{x}, \mathbf{y}) = \frac{1}{2} \|\mathbf{x} - \mathbf{y}\|_2^2$ , there exists a convex function  $u : \Omega \rightarrow \mathbb{R}$  such that its gradient  $\nabla u$  uniquely solves (6) (Brenier 1991), i.e.,  $M_{ot} = \nabla u$ . This shows that the OT map is the gradient of Brenier’s potential. As noted in (Lei et al. 2020; An et al. 2020),  $u$  can be represented as the upper envelope of hyperplanes  $\pi_{\mathbf{h}, i}(\mathbf{x}) = \langle \mathbf{x}, \mathbf{y}_i \rangle + h_i$ , and is uniquely parameterized (up to an additive constant) by a height vector  $\mathbf{h} = (h_1, h_2, \dots, h_{|\mathcal{I}|})^T$ . The resulting potential, denoted  $u_{\mathbf{h}}$ , is given by:

$$u_{\mathbf{h}}(\mathbf{x}) = \max_{i \in \mathcal{I}} \{\pi_{\mathbf{h}, i}(\mathbf{x})\}, u_{\mathbf{h}} : \Omega \rightarrow \mathbb{R}^n. \quad (7)$$

Given the target measure  $\nu$ , there exists a Brenier potential  $u_{\mathbf{h}}$  (as in (7)) such that the projected volume under each support plane matches the prescribed mass  $\nu_i$ . To obtain  $u_{\mathbf{h}}$ ,

it suffices to optimize the height vector  $\mathbf{h}$  by minimizing the following convex energy function:

$$E(\mathbf{h}) = \int_0^{\mathbf{h}} \sum_{i \in \mathcal{I}} w_i(\gamma) d\gamma_i - \sum_{i \in \mathcal{I}} h_i \nu_i, \quad (8)$$

where  $w_i(\gamma)$  is the  $\mu$ -volume of  $W_i(\gamma)$ . For more theoretical details, we refer to Reference (Gu et al. 2013).

### Related works

This section presents a curated overview of relevant literature, with additional references available in *Appendix A* and in the review articles (Hoyez et al. 2022; Huang et al. 2024).

**Conditional guided and controlled translation.** To enhance control over image generation, researchers have proposed multimodal conditional strategies using text, exemplars, or semantic labels. Kim et al. (Kim, Kwon, and Ye 2022) applied DMs with CLIP loss for text-guided editing, while Meng et al. (Meng et al. 2021) synthesized realistic images by adding noise to images and denoising via reverse-time SDEs. Tumanyan et al. (Tumanyan et al. 2023) enabled fine-grained control by manipulating internal features of pre-trained models. Seo et al. (Seo et al. 2023) improved exemplar-guided accuracy via alternating cross-domain matching and latent diffusion. Cheng et al. (Cheng et al. 2023) addressed single-example translation through content-concept inversion and fusion. Classifier-free guidance was adopted in (Yang et al. 2023; Zhang et al. 2023b) for controlled editing. Kwon et al. (Kwon and Ye 2022) performed text- and image-guided style transfer by aligning attention keys and class tokens, while Shi et al. (Shi et al. 2024b) introduced latent optimization with reference latent control for point-interactive editing.

**Efficient and lightweight translation.** To mitigate the high computational cost of DMs, various optimization strategies have been explored. Song et al. (Song, Meng, and Ermon 2021) introduced non-Markovian sampling to reduce generation steps, while Luo et al. (Luo et al. 2023) achieved single-step inference via consistency distillation. Xia et al. (Xia et al. 2024a) proposed compact prior networks and dynamic transformers, and Jiang et al. (Jiang et al. 2024; Xia et al. 2024b) optimized time-step usage to accelerate translation. Parmar et al. (Parmar et al. 2024) combined single-step DMs with adversarial learning for fast, high-quality synthesis. Lee et al. (Lee, Jeong, and Sohn 2024) employed Brownian bridge strategies for better stability and efficiency. Additionally, Lee et al. (Lee, Kang, and Han 2024) improved text-driven I2I translation by interpolating prompts to refine noise prediction in pre-trained DMs.

### Methodology of OT-ALD

We use superscripts <sup>A</sup> and <sup>B</sup> to indicate their association with the source and target domains, respectively. Fig.8 illustrates the essential differences between OT-ALD and DDIB-based methods (Su et al. 2022; Yu et al. 2023; Zhang et al. 2023a; Popov et al. 2023; Zhang et al. 2024; Bourou et al. 2024; Hur et al. 2024; Yin et al. 2024; Mancusi et al. 2024).

Given an initial image distribution  $p_0^A$  in the source domain, DDIB-based methods advocate using the forward process of  $DM^A$  to corrode  $p_0^A$  into a latent code distribution  $p_T^A$ . The reverse process of  $DM^B$  then reconstructs the target image distribution  $p_0^B$  from  $p_T^A$ . According to the contraction property of SDEs, as illustrated in Fig.1(b), the Wasserstein distance  $\mathcal{W}_2(p_T^A, p_T^B)$  converges exponentially to zero as  $T \rightarrow +\infty$  (Khruikov et al. 2022; Franzese et al. 2023). However, in practical scenarios with finite  $T$ , we have  $\mathcal{W}_2(p_T^A, p_T^B) \neq 0$ , resulting in a mismatch between latent code distributions. Here we present Theorem 1, which demonstrates that this mismatch leads to deviations in the translation trajectory within the target domain, ultimately preventing the attainment of the desired target distribution. The proof can be found in *Appendix D.1*.

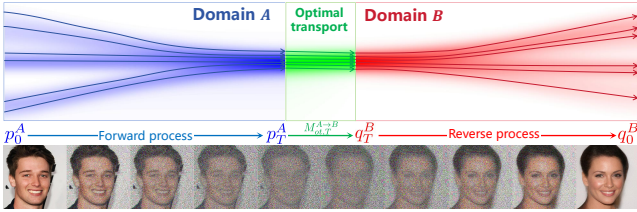


Fig 2: The framework of OT-ALD. During training, two DMs are independently trained in domains  $A$  and  $B$ , followed by computation of the OT map  $M_{ot,T}^{A \rightarrow B}$  from  $p_T^A$  to  $p_T^B$ . In translation, the source distribution  $p_0^A$  is diffused to  $p_T^A$ , which is then mapped via  $M_{ot,T}^{A \rightarrow B}$  to serve as the initial distribution for the reverse process in domain  $B$ , yielding the translated distribution  $q_0^B$ . In contrast, DDIB-based methods skip OT alignment and directly use  $p_T^A$ , leading to latent distribution mismatch. As shown in Theorem 1, this mismatch introduces a theoretical gap that affects target translation accuracy.

**Theorem 1.** *If  $q_T^B = p_T^A$ , we denote  $q_0^B$  as the distribution generated by the  $DM^B$ , then  $\mathcal{W}_2(p_0^B, q_0^B)$  can be estimated as follows*

$$\bar{I}^B(T) \mathcal{W}_2(p_T^A, p_T^B) \leq \mathcal{W}_2(p_0^B, q_0^B) \leq I^B(T) \mathcal{W}_2(p_T^A, p_T^B),$$

where  $I^B(T) = \exp\left(\int_0^T (L_f^B(t) + \frac{g^B(t)^2}{2} L_{S_\theta}^B(t)) dt\right)$  and  $\bar{I}^B(T) = \exp\left(\frac{1}{2} \int_0^T L_f^B(t) dt\right)$ ,  $L_f^B(t)$  and  $L_{S_\theta}^B(t)$  mean the continuous Lipschitz constant shown in *Appendix B*.

Theorem 1 states that for DDIB-based methods whenever  $\mathcal{W}_2(p_T^A, p_T^B) \neq 0$  holds,  $\mathcal{W}_2(p_0^B, q_0^B) \neq 0$  must follow. To address this theoretical gap, we compute the OT map  $M_{ot,T}^{A \rightarrow B}$  to align the source domain latent code distribution  $p_T^A$  with the target domain latent code distribution  $p_T^B$  (See Algorithm 1). We then use  $M_{ot,T}^{A \rightarrow B}(p_T^A)$  as the initial distribution for the reverse process of  $DM^B$ , effectively eliminating the discrepancy caused by latent code distribution mismatch. Furthermore, we provide an error estimation in Theorem 2. The proof can be found in *Appendix D.2*.

**Theorem 2.** *The error upper bound between the distribution obtained by OT-ALD and the ground truth is*

$$\mathcal{W}_2(p_0^B, q_0^B) \leq \sqrt{2T} (\mathcal{J}_{SM}^B)^{\frac{1}{2}} + KI^B(T) \|u_T^{A \rightarrow B} - u_h\|_{\infty}^{\frac{1}{2}},$$

where  $K$  is a positive constant and  $u_T^{A \rightarrow B}$  is the true Brenier function between  $p_T^A$  and  $p_T^B$ .

It is worth noting that the noise scaling factor  $\eta \in [0, 1]$  in (4) determines whether the diffusion process is Markovian or non-Markovian by controlling the noise added during sampling (Song, Meng, and Ermon 2021). When  $\eta \rightarrow 1$ , our model generates images with greater diversity. Conversely, as  $\eta \rightarrow 0$ , it produces images more quickly and with higher determinism (See Fig. 3(a)).

**Complexity analysis.** In Algorithm 1, the complexity of determining the cell to which each point in set  $\mathcal{X}_T^A$  belongs is  $\mathcal{O}(|\mathcal{K}||\mathcal{I}|)$ . Subsequently, the complexity of calculating the measure of a cell based on the points belonging to it is  $\mathcal{O}(|\mathcal{K}||\mathcal{I}|)$ . Assuming the number of iterations in Algorithm 1 is  $N$ , the complexity introduced by the Adam algorithm is  $\mathcal{O}(N|\mathcal{I}|)$ . Therefore, the total complexity of computing OT is  $\mathcal{O}((2|\mathcal{K}| + N)|\mathcal{I}|)$ .

---

Algorithm 1: Computing OT between latent distributions.

---

**Input:** Source images  $\mathcal{X}_0^A = \{\mathbf{x}_{0,k}^A\}_{k \in \mathcal{K}} \sim p_0^A$ , target images  $\mathcal{X}_0^B = \{\mathbf{x}_{0,i}^B\}_{i \in \mathcal{I}} \sim p_0^B$ , trained  $\mathbf{S}_\theta^A$  and  $\mathbf{S}_\theta^B$ , diffusion termination time  $T$ .

**Output:** OT map  $M_{ot,T}^{A \rightarrow B}$ .

- 1:  $\mathcal{X}_T^A \leftarrow \text{Solver}_\eta(\mathcal{X}_0^A, \mathbf{S}_\theta^A, 0, T)$ .
- 2:  $\mathcal{X}_T^B \leftarrow \text{Solver}_\eta(\mathcal{X}_0^B, \mathbf{S}_\theta^B, 0, T)$ .
- 3:  $\mathbf{h} \leftarrow \mathbf{0}$ .
- 4: **repeat**
- 5:   Calculate  $\nabla E(\mathbf{h}) = (w_i(\mathbf{h}) - \nu_i)^T$ .
- 6:    $\nabla E(\mathbf{h}) = \nabla E(\mathbf{h}) - \text{mean}(\nabla E(\mathbf{h}))$ .
- 7:   Update  $\mathbf{h}$  by Adam algorithm with  $\beta_1 = 0.9$ ,  $\beta_2 = 0.5$ .
- 8: **until** Converge
- 9:  $M_{ot,T}^{A \rightarrow B} \leftarrow \nabla u_h, u_h(\cdot) = \max_i \langle \cdot, \mathbf{x}_{T,i}^B \rangle + h_i$ .

**Return:**  $M_{ot,T}^{A \rightarrow B}$ .

---



---

Algorithm 2: I2I translation process of OT-ALD.

---

**Input:** Source image  $\mathbf{x}_0^A \sim p_0^A$ , computed OT map  $M_{ot,T}^{A \rightarrow B}$ , trained score networks  $\mathbf{S}_\theta^A(\mathbf{x}^A, t)$  and  $\mathbf{S}_\theta^B(\mathbf{x}^B, t)$ , noise scaling factor  $\eta$ .

**Output:** Target image  $\mathbf{x}_0^B$ .

- 1:  $\mathbf{x}_T^A \leftarrow \text{Solver}_\eta(\mathbf{x}_0^A, \mathbf{S}_\theta^A, 0, T)$ .
- 2:  $\mathbf{x}_T^B \leftarrow M_{ot,T}^{A \rightarrow B}(\mathbf{x}_T^A)$ .
- 3:  $\mathbf{x}_0^B \leftarrow \text{Solver}_\eta(\mathbf{x}_T^B, \mathbf{S}_\theta^B, T, 0)$ .

**Return:**  $\mathbf{x}_0^B$ .

---

Therefore, the OT-ALD consists of three stages: (1) Compute the latent code  $\mathbf{x}_T^A$  by applying the forward process of  $DM^A$  to degrade the source image  $\mathbf{x}_0^A$ . (2) Obtain the latent code  $\mathbf{x}_T^B$  in the target domain corresponding to  $\mathbf{x}_T^A$  under OT map  $M_{ot,T}^{A \rightarrow B}$ . (3) Generate the target image  $\mathbf{x}_0^B$  by applying the reverse process of  $DM^B$  to reconstruct  $\mathbf{x}_T^B$ . The complete translation process is outlined in Algorithm 2.

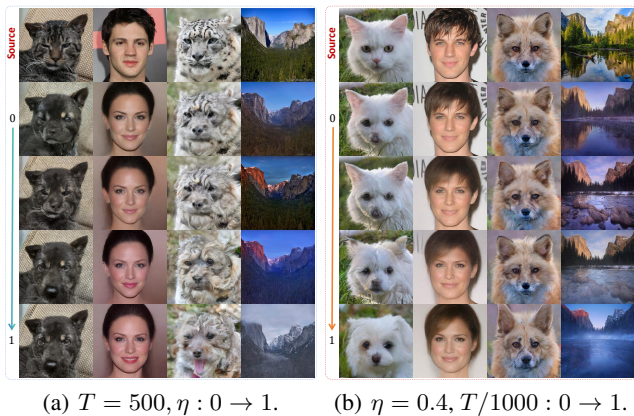


Fig 3: The smaller the adopted  $\eta$  and  $T$ , the higher the fidelity of OT-ALD to the source image is maintained; Conversely, larger values of  $\eta$  and  $T$  indicate that OT-ALD can achieve greater diversity in I2I translation tasks.

Building on its ability to eliminate latent code distribution mismatch, OT-ALD can be naturally extended to accelerated I2I translation by reducing the diffusion termination time  $T$ . Fig. 3(b) highlights that OT-ALD with a smaller  $T$  better preserves the details and structural integrity of the source image, while a larger  $T$  leverages the strengths of DM to enhance the diversity of the translated image. Therefore, an appropriate value of  $T$  must be selected to strike a balance between computational efficiency and output quality.

Theoretically, OT-ALD satisfies cycle consistency, which we explain from two different perspectives: sample-level (Theorem 3) and distribution-level (Theorem 4). Notably, sample-level cycle consistency holds only when  $\eta = 0$  in Algorithm 2. However, once stochasticity is introduced, this desirable property no longer holds. In contrast, distribution-level cycle consistency remains valid for  $\forall \eta \in [0, 1]$  under the control of FPE (2).

**Theorem 3** (Sample cycle consistency). *Disregarding the score matching error, the discretization error of the Solver $_{\eta}$  and the computational error of the OT map,  $\eta = 0$ . For any given  $T \geq 0$  and source image  $\mathbf{x}_0^A$ , we consider the following cyclic process*

$$\begin{aligned} \mathbf{x}_T^A &= \text{Solver}_{\eta}(\mathbf{x}_0^A, \mathbf{S}_{\theta}^A, 0, T), \mathbf{x}_T^B = M_{ot,T}^{A \rightarrow B}(\mathbf{x}_T^A), \\ \mathbf{x}_0^B &= \text{Solver}_{\eta}(\mathbf{x}_T^B, \mathbf{S}_{\theta}^B, T, 0), \mathbf{x}_T^B = \text{Solver}_{\eta}(\mathbf{x}_T^B, \mathbf{S}_{\theta}^B, 0, T), \\ \mathbf{x}_T^A &= M_{ot,T}^{B \rightarrow A}(\mathbf{x}_T^B), \mathbf{x}_0^A = \text{Solver}_{\eta}(\mathbf{x}_T^A, \mathbf{S}_{\theta}^A, T, 0), \end{aligned}$$

where  $M_{ot,T}^{B \rightarrow A} = (M_{ot,T}^{A \rightarrow B})^{-1}$ , then  $\|\mathbf{x}_0^A - \mathbf{x}_0^A\|_2 = 0$  holds. See Appendix D.3 for the proof detail.

**Theorem 4** (Distributional cycle consistency). *Under the same setting as Theorem 3, we apply the proposed method to translate the source distribution  $p_0^A$  into the target distribution. Subsequently, the approximate source distribution  $p_0^A$  derived from the reverse translation action on the target distribution. Then we have  $\mathcal{W}_2(p_0^A, p_0^A) = 0$  for  $\forall \eta \in [0, 1]$ . See Appendix D.4 for the proof detail.*

Sample consistency forms the basis of distribution consistency—when all individuals satisfy cycle consistency, the

distribution naturally aligns. However, distribution consistency does not require strict reversibility of individual samples, making it more flexible and tolerant of individual differences to improve overall distribution alignment.



Fig 4: The flexibility tests of OT-ALD on the trained DMs and OT map. Top-row images are sources; bottom-row images are the corresponding outputs generated by OT-ALD.

Moreover, OT-ALD is based on independently trained DMs and OT map, thereby inheriting the strong flexibility advantages of DDIB-based methods. To validate this property, we recombine the trained DMs in a manner different from the four main experiments. As shown in Fig. 4, OT-ALD still achieves high-quality translation results under this setting. Notably, as shown in the "Wild→Wild" results in Fig. 4, when the target image dataset is the same as the source image dataset, our model can achieve the effect of detail enhancement.

## Experiments

### Implementation details

**Datasets.** We evaluate four I2I translation tasks on three public datasets. (1) The AFHQ dataset (Choi et al. 2020) is a  $512 \times 512$  animal face dataset containing approximately 5,000 images per class (cat, dog, wild), used for Cat→Dog and Wild→Dog translation. (2) The Summer2Winter dataset (Zhu et al. 2017) consists of  $256 \times 256$  seasonal landscape images under varying weather and lighting conditions, used for Summer→Winter translation. (3) The CelebA-HQ dataset (Karras et al. 2017) includes 30,000 facial images (resized to  $512 \times 512$ ) with diverse attributes and poses, used for Male→Female translation.

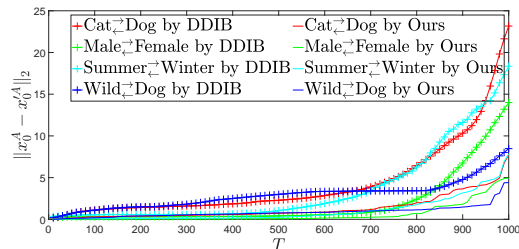
**Baseline models.** In this work, we compare our model with the following methods: CUT (Park et al. 2020), EGSDE (Zhao et al. 2022), ILVR (Choi et al. 2021), SDEdit (Meng et al. 2021), StarGANv2 (Choi et al. 2020), SDDM (Sun et al. 2023), InjectDiff (Li and Ma 2023), CycleGAN (Zhu et al. 2017), QS-Attn (Hu et al. 2022), DDIB (Su et al. 2022), InstPix2Pix (Brooks, Holynski, and Efros 2023), Pix2Pix-Zero (Parmar et al. 2023), P2P (Hertz et al. 2022), UNSB (Kim et al. 2023), GcGAN (Fu et al. 2019), DistanceGAN (Benaim and Wolf 2017), Plug&Play (Tumanyan et al. 2023), CycleDiff (Wu and De la Torre 2023), Turbo (Parmar et al. 2024), U-GAT-IT (Kim et al. 2019), NICE-GAN (Chen et al. 2020), DDIB (Su et al. 2022; Yu et al. 2023; Popov et al. 2023; Zhang et al. 2024; Bourou et al. 2024; Hur et al. 2024; Yin et al. 2024; Mancusi et al. 2024), DMT (Xia et al. 2024b).

**Evaluation metrics.** For the translated images, we evaluate realism using Fréchet Inception Distance (FID) (Heusel

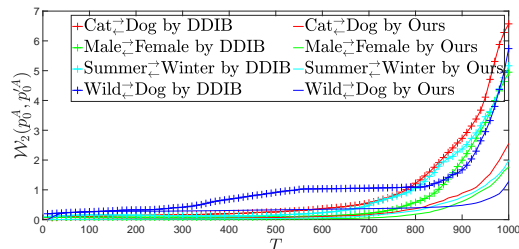
et al. 2017), Kernel Inception Distance (KID) (Bińkowski et al. 2018) and Fool rates (Saharia et al. 2022b). To measure faithfulness, we employ  $L_2$  distance, Peak Signal-to-Noise Ratio (PSNR), Structural Similarity Index Measure (SSIM) (Wang et al. 2004), and DINO-Struct-Dist (Tumanyan et al. 2022). Additionally, the Wasserstein distance  $\mathcal{W}_2(p_T^B, q_T^B)$  quantifies the latent code distribution matching error of the proposed method and DDIB-based approach. Finally, we assess computational efficiency by comparing translation time (s/image) across different models.

More experimental configuration details can be found in Appendix E.1.

### Mismatch within latent code distributions and cycle consistency



(a) Sample cycle consistency



(b) Distribution cycle consistency

Fig 5: Comparison of cycle consistency between OT-ALD and DDIB-based methods.

For the four I2I translation tasks, Fig. 1(b) shows the latent distribution mismatch for our method and the DDIB-based approach. The results confirm that introducing the OT map effectively eliminates this discrepancy, yielding a target distribution closer to the ground truth (see Fig. 1(c), Theorems 1–2). We further analyze the effect of varying diffusion termination time  $T$ , showing that our method is less sensitive to  $T$  than DDIB, which requires a longer diffusion process to compensate for the mismatch—at the cost of significantly lower sampling efficiency.

Subsequently, we evaluate the cycle consistency of our method and DDIB-based approach in Figs. 5(a) and 5(b). Although both methods theoretically satisfy sample-level and distribution-level cycle consistency (Theorems 3–4), the large number of diffusion steps in the DDIB-based method leads to accumulated computational errors, resulting in inferior cycle consistency compared to our model.

Table 1: Quantitative comparison on four tasks.  $\uparrow$  and  $\downarrow$  indicate directions of better values, where the optimal value is marked in **bold** and the suboptimal is marked with underline.

Methods	Cat→Dog			
	FID $\downarrow$	$L_2\downarrow$	PSNR $\uparrow$	SSIM $\uparrow$
CUT	76.21	59.78	17.48	<b>0.601</b>
StarGANv2	54.88	133.65	10.63	0.27
CycleGAN	85.90	—	18.13	<u>0.58</u>
QS-Attn	72.80	—	18.26	0.39
SDEdit	74.14	47.88	19.19	0.423
SDDM	62.29	—	—	0.422
SDDM $\dagger$	49.43	—	—	0.361
InjectDiff	63.76	—	20.10	0.48
ILVR	74.37	56.95	17.77	0.363
EGSDE	65.82	47.22	19.31	0.415
EGSDE $\dagger$	51.04	62.02	17.17	0.361
DMT	<u>47.86</u>	<u>45.98</u>	<u>20.55</u>	0.412
DDIB	59.62	60.23	18.91	0.372
OT-ALD	<b>44.31</b>	<b>42.35</b>	<b>21.20</b>	0.470

Methods	Wild→Dog			
	FID $\downarrow$	$L_2\downarrow$	PSNR $\uparrow$	SSIM $\uparrow$
CUT	92.94	62.21	17.20	<b>0.592</b>
ILVR	75.33	63.40	16.85	0.287
SDEdit	68.51	55.36	17.98	0.343
EGSDE	59.75	54.34	18.14	0.343
EGSDE $\dagger$	50.43	66.52	16.40	0.300
SDDM $\dagger$	57.38	—	—	0.328
DMT	49.83	52.42	18.05	0.338
DDIB	55.34	60.01	17.72	0.332
OT-ALD	<b>47.65</b>	<b>50.03</b>	<b>18.95</b>	<u>0.351</u>

Methods	Male→Female			
	FID $\downarrow$	$L_2\downarrow$	PSNR $\uparrow$	SSIM $\uparrow$
CUT	31.94	46.61	19.87	0.74
ILVR	46.12	52.17	18.59	0.510
SDEdit	49.43	43.70	20.03	0.572
EGSDE	41.93	42.04	20.35	0.574
EGSDE $\dagger$	30.61	53.44	18.32	0.510
InjectDiff	<u>28.12</u>	—	21.65	0.67
CycleGAN	36.75	—	21.54	0.70
QS-Attn	32.56	—	20.68	0.60
SDDM	44.37	—	—	0.526
DMT	29.01	35.63	22.42	0.687
DDIB	38.25	38.55	21.37	0.66
OT-ALD	<b>25.21</b>	<b>31.51</b>	<b>23.05</b>	<b>0.75</b>

Methods	Summer→Winter		
	FID $\downarrow$	KID $\downarrow$	DINO Struct. $\downarrow$
CycleGAN	62.9	1.022	2.6
DistanceGAN	97.2	2.843	—
GcGAN	97.5	2.755	—
CUT	72.1	1.207	2.1
SDEdit	66.1	3.218	2.1
Plug&Play	67.3	—	2.8
CycleDiff	64.1	—	3.6
P2P	99.1	2.626	—
Pix2Pix-Zero	68.0	—	3.0
InstPix2Pix	68.3	—	3.7
UNSB	73.9	<b>0.421</b>	—
DDIB	90.8	2.36	7.2
Turbo	56.3	—	<b>0.6</b>
NiceGAN	76.03	0.67	—
NiceGAN $\dagger$	77.13	0.73	—
U-GAT-IT	88.41	1.43	—
EGSDE	62.38	0.75	1.8
ILVR	65.64	1.35	2.0
DMT	<u>54.64</u>	0.564	1.7
OT-ALD	<b>52.87</b>	<u>0.521</u>	<u>1.5</u>

## Image realism and faithfulness

Tab. 1 reports the quantitative results of OT-ALD ( $T = 500$ ,  $\eta = 0.2$ ) and baseline models across four I2I translation tasks. Compared to other methods, OT-ALD not only preserves the structural integrity of the source images but also achieves the highest output quality. Across these four tasks,

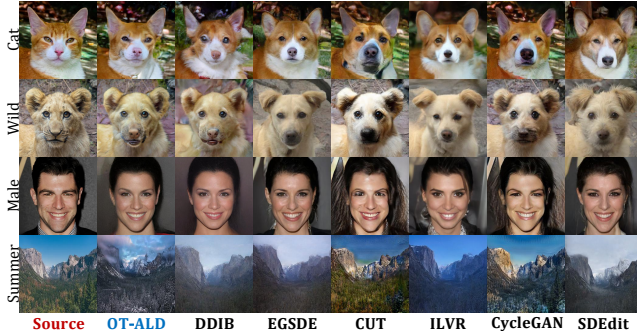


Fig 6: Visualization comparison of different models over four I2I translation tasks. Compared with other mainstream methods, OT-ALD has the highest fidelity to source images, and its output quality is on par with or even superior to them.

the FID value of our model is 2.6 lower on average than that of the optimal model in each corresponding task. Furthermore, Fig. 6 provides a visual comparison between OT-ALD and representative I2I approaches, demonstrating that our model generates clearer and more realistic results than its counterparts, while largely maintaining the structure of the source image.

Human evaluations offer a more accurate assessment of I2I translation quality. As shown in (Mantiuk, Tomaszewska, and Mantiuk 2012), forced pairwise comparison is a reliable method for image quality evaluation. Accordingly, we adopt the 2-alternative forced-choice (2AFC) paradigm (Zhang, Isola, and Efros 2016), where 50 participants are shown 20 randomly selected image pairs, each consisting of a generated image (from the source domain) and its corresponding real target image. Participants are informed that only one image per pair is real and are asked to choose the one they believe is real. The proportion of a generated image is mistakenly selected—Fool Rate—is recorded. The Fool Rate value closer to 50% indicates higher image realism, while a lower rate suggests more noticeable artifacts.

Table 2: Comparison of average Fool Rates ( $\uparrow$ ) of different methods.

Methods	Cat→Dog	Wild→Dog	Summer→Winter	Male→Female
CUT	23.6%	22.3%	29.9%	28.5%
CycleGAN	22.3%	25.4%	34.5%	23.7%
ILVR	21.4%	24.1%	23.3%	29.2%
EGSDE	24.1%	<b>28.3%</b>	26.6%	27.2%
DDIB	18.5%	19.9%	30.8%	25.9%
SDEdit	20.7%	21.5%	33.4%	24.4%
DMT	<b>24.3%</b>	25.7%	33.9%	27.5%
OT-ALD	22.8%	26.9%	<b>37.2%</b>	<b>29.4%</b>

Fig. 7 shows examples generated by OT-ALD with their corresponding average Fool Rates. Some results from the

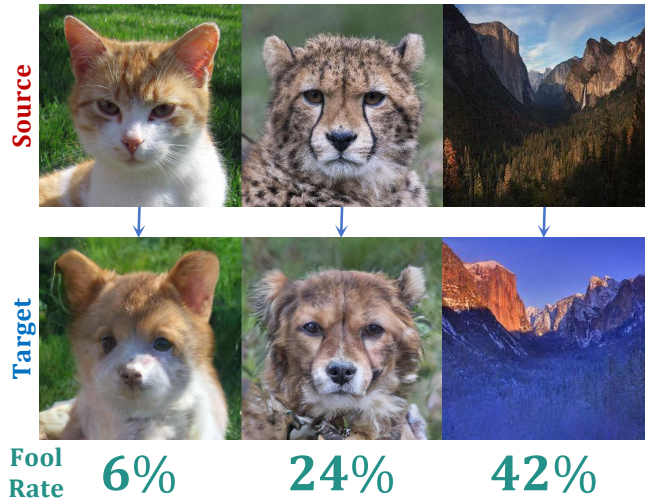


Fig 7: Visualization comparison of Fool Rate. The Fool rate essentially reflects the difficulty in distinguishing between translated images and real images. The larger the value of this metric and the closer it is to 50%, the stronger the realism of the images.

summer-to-winter task achieve rates above 40%, indicating high realism, while some distorted images score near 0%. Tab. 2 compares the average Fool Rates of our model with others across four tasks, where our model consistently achieves around 29%, suggesting it often produces images that are partially indistinguishable from real ones.

## Translation efficiency

To evaluate the computational efficiency of different models on various translation tasks, we first fully train them on a single RTX 4090 GPU. Then, for each task, we randomly select 1000 source images and measure the average GPU time required by each model to translate them into target images. The results in Tab. 3 demonstrate that OT-ALD is more efficient than other diffusion-based I2I translation technologies under same conditions. This advantage mainly stems from the reduced  $T$  required by our model.

Table 3: Translating time comparison (s/image,  $\downarrow$ ) of different *diffusion-based* models *under same conditions*. The corresponding FID scores ( $\downarrow$ ) are indicated in parentheses. Our model adopts  $T = 500$  and  $\eta = 0.2$ . The average sampling time of our model across four tasks is 20.29% lower than that of the model with the best translation efficiency (ILVR).

Methods	Cat→Dog	Wild→Dog	Summer→Winter	Male→Female
EGSDE	79.85 (51.04)	79.75 (40.43)	19.06 (62.38)	79.80 (30.61)
ILVR	52.31 (70.37)	52.26 (75.33)	16.97 (65.64)	52.58 (46.12)
DDIB	92.30 (59.62)	92.36 (55.34)	20.64 (90.80)	92.35 (38.25)
DMT	75.20 (47.86)	74.98 (49.83)	18.85 (54.64)	75.25 (29.01)
SDEdit	86.44 (74.14)	87.12 (68.51)	19.85 (66.10)	86.77 (49.43)
OT-ALD	<b>45.15 (44.31)</b>	<b>45.18 (47.65)</b>	<b>10.21 (52.87)</b>	<b>45.18 (25.21)</b>

In addition to keeping the experimental equipment consistent, when testing the translating time in Tab. 3, we adopted the same sampling method for all diffusion-based models

and did not use any acceleration strategies for the diffusion process. This means that if an acceleration strategy is introduced, all time data in Tab. 3 will decrease synchronously, while our model will still outperform other baseline models.

### **Ablation study**

(1) **Optimal Transport.** Figs. 1(b)-1(c) and Fig. 5 compare the classical DDIB-based method and OT-ALD in terms of latent distribution alignment, translated target distribution, and cycle consistency, along with their variations over diffusion termination time  $T$ .

(2) **Noise Scale Factor  $\eta$ .** Fig. 3(a) illustrates the impact of  $\eta$  on OT-ALD. With fixed  $T$ , a larger  $\eta$  leads to improved output quality and diversity.

(3) **Diffusion termination time  $T$ .** Fig. 3(b) demonstrates the effect of  $T$  on OT-ALD. When  $\eta$  is fixed and positive, increasing  $T$  enhances both generation quality and diversity. Moreover, for fixed-size image tasks, the average translation time of OT-ALD increases linearly with  $T$ .

### **Conclusion**

This paper provides a theoretical analysis of the limitations of classical DDIB-based I2I translation methods, namely: (1) low efficiency during the translation process and (2) translation trajectory deviations due to mismatched latent distributions. To address these issues, we propose OT-ALD, which effectively eliminates latent distribution mismatch, and offers theoretical guarantees for key properties such as cycle consistency. In practice, OT-ALD enables fast, high-quality image translation with flexible control over transformation objectives, allowing users to balance generation speed and synthesis quality according to their specific needs.

### **Acknowledgments**

This research was supported by the National Key Research and Development Program of China under Grant No. 2021YFA1003003; the National Natural Science Foundation of China under Grant No. T2225012.

## References

- An, D.; Guo, Y.; Lei, N.; Luo, Z.; Yau, S.-T.; and Gu, X. 2020. AE-OT: A New Generative Model Based on Extended Semi-Discrete Optimal Transport. In *Proceedings of the 8th International Conference on Learning Representations*.
- Anderson, B. D. 1982. Reverse-time diffusion equation models. *Stochastic Processes and their Applications*, 12(3): 313–326.
- Azadi, S.; Fisher, M.; Kim, V. G.; Wang, Z.; Shechtman, E.; and Darrell, T. 2018. Multi-content gan for few-shot font style transfer. In *Proceedings of the IEEE conference on computer vision and pattern recognition*, 7564–7573.
- Bai, X.; Pu, X.; and Xu, F. 2023. Conditional Diffusion for SAR to Optical Image Translation. *IEEE Geoscience and Remote Sensing Letters*.
- Bai, X.; and Xu, F. 2024. Sar to optical image translation with color supervised diffusion model. In *IGARSS 2024-2024 IEEE International Geoscience and Remote Sensing Symposium*, 963–966. IEEE.
- Benaim, S.; and Wolf, L. 2017. One-sided unsupervised domain mapping. *Advances in neural information processing systems*, 30.
- Bińkowski, M.; Sutherland, D. J.; Arbel, M.; and Gretton, A. 2018. Demystifying mmd gans. *arXiv preprint arXiv:1801.01401*.
- Bourou, A.; Boyer, T.; Gheisari, M.; Daupin, K.; Dubreuil, V.; De Thonel, A.; Mezger, V.; and Genovesio, A. 2024. PhenDiff: Revealing subtle phenotypes with diffusion models in real images. In *International Conference on Medical Image Computing and Computer-Assisted Intervention*, 358–367. Springer.
- Brenier, Y. 1991. Polar factorization and monotone rearrangement of vector-valued functions. *Communications on pure and applied mathematics*, 44: 375–417.
- Brooks, T.; Holynski, A.; and Efros, A. A. 2023. Instruct-pix2pix: Learning to follow image editing instructions. In *Proceedings of the IEEE/CVF conference on computer vision and pattern recognition*, 18392–18402.
- Carrillo, J. A.; McCann, R. J.; and Villani, C. 2006. Contractions in the 2-Wasserstein length space and thermalization of granular media. *Archive for Rational Mechanics and Analysis*, 179: 217–263.
- Ceylan, D.; Huang, C.-H. P.; and Mitra, N. J. 2023. Pix2video: Video editing using image diffusion. In *Proceedings of the IEEE/CVF International Conference on Computer Vision*, 23206–23217.
- Chazal, F.; Cohen-Steiner, D.; Lieutier, A.; Mérigot, Q.; and Thibert, B. 2017. Inference of curvature using tubular neighborhoods. *Modern Approaches to Discrete Curvature*, 133–158.
- Chen, R.; Huang, W.; Huang, B.; Sun, F.; and Fang, B. 2020. Reusing discriminators for encoding: Towards unsupervised image-to-image translation. In *Proceedings of the IEEE/CVF conference on computer vision and pattern recognition*, 8168–8177.
- Chen, Y. ????. ContourDiff: Unpaired Image-to-Image Translation with Structural Consistency for Medical Imaging. In *Medical Imaging with Deep Learning*.
- Cheng, B.; Liu, Z.; Peng, Y.; and Lin, Y. 2023. General image-to-image translation with one-shot image guidance. In *Proceedings of the IEEE/CVF International Conference on Computer Vision*, 22736–22746.
- Choi, J.; Kim, S.; Jeong, Y.; Gwon, Y.; and Yoon, S. 2021. Ilvr: Conditioning method for denoising diffusion probabilistic models. *arXiv preprint arXiv:2108.02938*.
- Choi, Y.; Uh, Y.; Yoo, J.; and Ha, J.-W. 2020. Stargan v2: Diverse image synthesis for multiple domains. In *Proceedings of the IEEE/CVF conference on computer vision and pattern recognition*, 8188–8197.
- Franzese, G.; Rossi, S.; Yang, L.; Finamore, A.; Rossi, D.; Filippone, M.; and Michiardi, P. 2023. How much is enough? a study on diffusion times in score-based generative models. *Entropy*, 25(4): 633.
- Fu, H.; Gong, M.; Wang, C.; Batmanghelich, K.; Zhang, K.; and Tao, D. 2019. Geometry-consistent generative adversarial networks for one-sided unsupervised domain mapping. In *Proceedings of the IEEE/CVF conference on computer vision and pattern recognition*, 2427–2436.
- Gao, X.; Xu, Z.; Zhao, J.; and Liu, J. 2024. Frequency-Controlled Diffusion Model for Versatile Text-Guided Image-to-Image Translation. In *Proceedings of the AAAI Conference on Artificial Intelligence*, volume 38, 1824–1832.
- Gatys, L. A.; Ecker, A. S.; and Bethge, M. 2016. Image style transfer using convolutional neural networks. In *Proceedings of the IEEE conference on computer vision and pattern recognition*, 2414–2423.
- Graf, R.; Schmitt, J.; Schlaeger, S.; Möller, H. K.; Sideri-Lampretsa, V.; Sekuboyina, A.; Krieg, S. M.; Wiestler, B.; Menze, B.; Rueckert, D.; et al. 2023. Denoising diffusion-based MRI to CT image translation enables automated spinal segmentation. *European Radiology Experimental*, 7(1): 70.
- Gu, X.; Luo, F.; Sun, J.; and Yau, S.-T. 2013. Variational principles for Minkowski type problems, discrete optimal transport, and discrete Monge-Ampere equations. *arXiv preprint arXiv:1302.5472*.
- Guo, Z.; Liu, J.; Cai, Q.; Zhang, Z.; and Mei, S. 2024. Learning SAR-to-optical image translation via diffusion models with color memory. *IEEE Journal of Selected Topics in Applied Earth Observations and Remote Sensing*.
- Han, C.; Liang, J. C.; Wang, Q.; Rabbani, M.; Dianat, S.; Rao, R.; Wu, Y. N.; and Liu, D. 2024. Image translation as diffusion visual programmers. *arXiv preprint arXiv:2401.09742*.
- Hertz, A.; Mokady, R.; Tenenbaum, J.; Aberman, K.; Pritch, Y.; and Cohen-Or, D. 2022. Prompt-to-prompt image editing with cross attention control. *arXiv preprint arXiv:2208.01626*.

- Heusel, M.; Ramsauer, H.; Unterthiner, T.; Nessler, B.; and Hochreiter, S. 2017. GANs trained by a two time-scale update rule converge to a local nash equilibrium. In *Proceedings of the 31st International Conference on Neural Information Processing Systems*, 6629–6640.
- Ho, J.; Jain, A.; and Abbeel, P. 2020. Denoising diffusion probabilistic models. In *Proceedings of the 34th International Conference on Neural Information Processing Systems*, 6840–6851.
- Hoyez, H.; Schockaert, C.; Rambach, J.; Mirbach, B.; and Stricker, D. 2022. Unsupervised image-to-image translation: A review. *Sensors*, 22(21): 8540.
- Hu, X.; Zhou, X.; Huang, Q.; Shi, Z.; Sun, L.; and Li, Q. 2022. Qs-attn: Query-selected attention for contrastive learning in i2i translation. In *Proceedings of the IEEE/CVF Conference on Computer Vision and Pattern Recognition*, 18291–18300.
- Huang, Y.; Huang, J.; Liu, Y.; Yan, M.; Lv, J.; Liu, J.; Xiong, W.; Zhang, H.; Chen, S.; and Cao, L. 2024. Diffusion model-based image editing: A survey. *arXiv preprint arXiv:2402.17525*.
- Hur, J.; Choi, J.; Han, G.; Lee, D.-J.; and Kim, J. 2024. Expanding expressiveness of diffusion models with limited data via self-distillation based fine-tuning. In *Proceedings of the IEEE/CVF Winter Conference on Applications of Computer Vision*, 5028–5037.
- Isola, P.; Zhu, J.-Y.; Zhou, T.; and Efros, A. A. 2017. Image-to-image translation with conditional adversarial networks. In *Proceedings of the IEEE conference on computer vision and pattern recognition*, 1125–1134.
- Jiang, H.; Imran, M.; Ma, L.; Zhang, T.; Zhou, Y.; Liang, M.; Gong, K.; and Shao, W. 2024. Fast-DDPM: Fast Denoising Diffusion Probabilistic Models for Medical Image-to-Image Generation. *arXiv e-prints*, arXiv–2405.
- Karras, T.; Aila, T.; Laine, S.; and Lehtinen, J. 2017. Progressive growing of gans for improved quality, stability, and variation. *arXiv preprint arXiv:1710.10196*.
- Khrulkov, V.; Ryzhakov, G.; Chertkov, A.; and Oseledets, I. 2022. Understanding DDPM Latent Codes Through Optimal Transport. In *The Eleventh International Conference on Learning Representations*.
- Kim, B.; Kwon, G.; Kim, K.; and Ye, J. C. 2023. Unpaired Image-to-Image Translation via Neural Schrödinger Bridge. *arXiv preprint arXiv:2305.15086*.
- Kim, G.; Kwon, T.; and Ye, J. C. 2022. Diffusionclip: Text-guided diffusion models for robust image manipulation. In *Proceedings of the IEEE/CVF conference on computer vision and pattern recognition*, 2426–2435.
- Kim, J.; Kim, M.; Kang, H.; and Lee, K. 2019. U-gat-it: Unsupervised generative attentional networks with adaptive layer-instance normalization for image-to-image translation. *arXiv preprint arXiv:1907.10830*.
- Kim, J.; and Park, H. 2024. Adaptive latent diffusion model for 3d medical image to image translation: Multi-modal magnetic resonance imaging study. In *Proceedings of the IEEE/CVF Winter Conference on Applications of Computer Vision*, 7604–7613.
- Kim, S.-H.; and Chung, D.-w. 2024. Conditional brownian bridge diffusion model for vhr sar to optical image translation. *arXiv preprint arXiv:2408.07947*.
- Kim, T.; Cha, M.; Kim, H.; Lee, J. K.; and Kim, J. 2017. Learning to discover cross-domain relations with generative adversarial networks. In *International conference on machine learning*, 1857–1865. PMLR.
- Kwon, D.; Fan, Y.; and Lee, K. 2022. Score-based generative modeling secretly minimizes the wasserstein distance. *Advances in Neural Information Processing Systems*, 35: 20205–20217.
- Kwon, G.; and Ye, J. C. 2022. Diffusion-based image translation using disentangled style and content representation. *arXiv preprint arXiv:2209.15264*.
- Lee, E.; Jeong, S.; and Sohn, K. 2024. EBDM: Exemplar-Guided Image Translation with Brownian-Bridge Diffusion Models. In *European Conference on Computer Vision*, 306–323. Springer.
- Lee, J.; Kang, M.; and Han, B. 2024. Diffusion-Based Image-to-Image Translation by Noise Correction via Prompt Interpolation. In *European Conference on Computer Vision*, 289–304. Springer.
- Lei, N.; An, D.; Guo, Y.; Su, K.; Liu, S.; Luo, Z.; Yau, S.-T.; and Gu, X. 2020. A geometric understanding of deep learning. *Engineering*, 6: 361–374.
- Li, B.; Xue, K.; Liu, B.; and Lai, Y.-K. 2023a. BbDM: Image-to-image translation with brownian bridge diffusion models. In *Proceedings of the IEEE/CVF conference on computer vision and pattern recognition*, 1952–1961.
- Li, L.; and Ma, L. 2023. Injecting-Diffusion: Inject Domain-Independent Contents into Diffusion Models for Unpaired Image-to-Image Translation. In *2023 IEEE International Conference on Multimedia and Expo (ICME)*, 282–287. IEEE.
- Li, Y.; Shao, H.-C.; Liang, X.; Chen, L.; Li, R.; Jiang, S.; Wang, J.; and Zhang, Y. 2023b. Zero-shot medical image translation via frequency-guided diffusion models. *IEEE transactions on medical imaging*.
- Liang, J.; Cao, J.; Sun, G.; Zhang, K.; Van Gool, L.; and Timofte, R. 2021. Swinir: Image restoration using swin transformer. In *Proceedings of the IEEE/CVF international conference on computer vision*, 1833–1844.
- Lin, Y.; Xian, X.; Shi, Y.; and Lin, L. 2024. Mirrordiffusion: stabilizing diffusion process in zero-shot image translation by prompts redescription and beyond. *IEEE Signal Processing Letters*.
- Lin, Y.; Zhang, S.; Yang, X.; Wang, X.; and Shi, Y. 2023. Regeneration learning of diffusion models with rich prompts for zero-shot image translation. *arXiv preprint arXiv:2305.04651*.
- Liu, F.; and Chang, X. 2024. IIDM: Image-to-Image Diffusion Model for Semantic Image Synthesis. *arXiv preprint arXiv:2403.13378*.
- Lugmayr, A.; Danelljan, M.; Romero, A.; Yu, F.; Timofte, R.; and Van Gool, L. 2022. Repaint: Inpainting using denoising diffusion probabilistic models. In *Proceedings of*

- the *IEEE/CVF conference on computer vision and pattern recognition*, 11461–11471.
- Luo, S.; Tan, Y.; Huang, L.; Li, J.; and Zhao, H. 2023. Latent consistency models: Synthesizing high-resolution images with few-step inference. *arXiv preprint arXiv:2310.04378*.
- Luo, Y.; Yang, Q.; Liu, Z.; Shi, Z.; Huang, W.; Zheng, G.; and Cheng, J. 2024. Target-Guided Diffusion Models for Unpaired Cross-modality Medical Image Translation. *IEEE Journal of Biomedical and Health Informatics*.
- Mancusi, M.; Halychanskyi, Y.; Cheuk, K. W.; Moliner, E.; Lai, C.-H.; Uhlich, S.; Koo, J.; Martínez-Ramírez, M. A.; Liao, W.-H.; Fabbro, G.; et al. 2024. Latent Diffusion Bridges for Unsupervised Musical Audio Timbre Transfer. *arXiv preprint arXiv:2409.06096*.
- Mantiuk, R. K.; Tomaszewska, A.; and Mantiuk, R. 2012. Comparison of four subjective methods for image quality assessment. In *Computer graphics forum*, volume 31, 2478–2491. Wiley Online Library.
- Meng, C.; He, Y.; Song, Y.; Song, J.; Wu, J.; Zhu, J.-Y.; and Ermon, S. 2021. Sdedit: Guided image synthesis and editing with stochastic differential equations. *arXiv preprint arXiv:2108.01073*.
- Mérogot, Q.; Delalande, A.; and Chazal, F. 2020. Quantitative stability of optimal transport maps and linearization of the 2-Wasserstein space. In *International Conference on Artificial Intelligence and Statistics*, 3186–3196. PMLR.
- Odena, A.; Olah, C.; and Shlens, J. 2017. Conditional image synthesis with auxiliary classifier gans. In *International conference on machine learning*, 2642–2651. PMLR.
- Park, T.; Efros, A. A.; Zhang, R.; and Zhu, J.-Y. 2020. Contrastive learning for unpaired image-to-image translation. In *Computer Vision—ECCV 2020: 16th European Conference, Glasgow, UK, August 23–28, 2020, Proceedings, Part IX 16*, 319–345. Springer.
- Parmar, G.; Kumar Singh, K.; Zhang, R.; Li, Y.; Lu, J.; and Zhu, J.-Y. 2023. Zero-shot image-to-image translation. In *ACM SIGGRAPH 2023 Conference Proceedings*, 1–11.
- Parmar, G.; Park, T.; Narasimhan, S.; and Zhu, J.-Y. 2024. One-step image translation with text-to-image models. *arXiv preprint arXiv:2403.12036*.
- Patil, S. S.; Rajak, R.; Ramteke, M.; and Rathore, A. S. 2025. MMIT-DDPM—Multilateral medical image translation with class and structure supervised diffusion-based model. *Computers in Biology and Medicine*, 185: 109501.
- Popov, V.; Amatov, A.; Kudinov, M.; Gogoryan, V.; Sadekova, T.; and Vovk, I. 2023. Optimal transport in diffusion modeling for conversion tasks in audio domain. In *ICASSP 2023-2023 IEEE International Conference on Acoustics, Speech and Signal Processing (ICASSP)*, 1–5. IEEE.
- Risken, H.; and Risken, H. 1996. *Fokker-planck equation*. Springer.
- Rombach, R.; Blattmann, A.; Lorenz, D.; Esser, P.; and Ommer, B. 2022. High-resolution image synthesis with latent diffusion models. In *Proceedings of the IEEE/CVF conference on computer vision and pattern recognition*, 10684–10695.
- Saharia, C.; Chan, W.; Chang, H.; Lee, C.; Ho, J.; Salimans, T.; Fleet, D.; and Norouzi, M. 2022a. Palette: Image-to-image diffusion models. In *ACM SIGGRAPH 2022 conference proceedings*, 1–10.
- Saharia, C.; Ho, J.; Chan, W.; Salimans, T.; Fleet, D. J.; and Norouzi, M. 2022b. Image super-resolution via iterative refinement. *IEEE transactions on pattern analysis and machine intelligence*, 45(4): 4713–4726.
- Sasaki, H.; Willcocks, C. G.; and Breckon, T. P. 2021. Unitddpm: Unpaired image translation with denoising diffusion probabilistic models. *arXiv preprint arXiv:2104.05358*.
- Seo, J.; Lee, G.; Cho, S.; Lee, J.; and Kim, S. 2023. Midms: Matching interleaved diffusion models for exemplar-based image translation. In *Proceedings of the AAAI Conference on Artificial Intelligence*, volume 37, 2191–2199.
- Shi, H.; Cui, Z.; Chen, L.; He, J.; and Yang, J. 2024a. A brain-inspired approach for SAR-to-optical image translation based on diffusion models. *Frontiers in Neuroscience*, 18: 1352841.
- Shi, Y.; Xue, C.; Liew, J. H.; Pan, J.; Yan, H.; Zhang, W.; Tan, V. Y.; and Bai, S. 2024b. Dragdiffusion: Harnessing diffusion models for interactive point-based image editing. In *Proceedings of the IEEE/CVF Conference on Computer Vision and Pattern Recognition*, 8839–8849.
- Song, J.; Meng, C.; and Ermon, S. 2021. Denoising Diffusion Implicit Models. In *International Conference on Learning Representations*.
- Song, Y.; Durkan, C.; Murray, I.; and Ermon, S. 2021. Maximum likelihood training of score-based diffusion models. *Advances in neural information processing systems*, 34: 1415–1428.
- Song, Y.; Sohl-Dickstein, J.; Kingma, D. P.; Kumar, A.; Ermon, S.; and Poole, B. 2020. Score-based generative modeling through stochastic differential equations. *arXiv preprint arXiv:2011.13456*.
- Su, X.; Song, J.; Meng, C.; and Ermon, S. 2022. Dual diffusion implicit bridges for image-to-image translation. *arXiv preprint arXiv:2203.08382*.
- Sun, S.; Wei, L.; Xing, J.; Jia, J.; and Tian, Q. 2023. SDDM: score-decomposed diffusion models on manifolds for unpaired image-to-image translation. In *International Conference on Machine Learning*, 33115–33134. PMLR.
- Tu, H.; Wang, Z.; and Zhao, Y. 2024. Unpaired image-to-image translation with diffusion adversarial network. *Mathematics*, 12(20): 3178.
- Tumanyan, N.; Bar-Tal, O.; Bagon, S.; and Dekel, T. 2022. Splicing vit features for semantic appearance transfer. In *Proceedings of the IEEE/CVF Conference on Computer Vision and Pattern Recognition*, 10748–10757.
- Tumanyan, N.; Geyer, M.; Bagon, S.; and Dekel, T. 2023. Plug-and-play diffusion features for text-driven image-to-image translation. In *Proceedings of the IEEE/CVF Conference on Computer Vision and Pattern Recognition*, 1921–1930.
- Vinholi, J. G.; Chini, M.; Amziane, A.; Machado, R.; Silva, D.; and Matgen, P. 2024. Multi-Sensor Diffusion-Driven

- Optical Image Translation for Large-Scale Applications. *IEEE Journal of Selected Topics in Applied Earth Observations and Remote Sensing*.
- Wang, T.; Zhang, T.; Zhang, B.; Ouyang, H.; Chen, D.; Chen, Q.; and Wen, F. 2022a. Pretraining is all you need for image-to-image translation. *arXiv preprint arXiv:2205.12952*.
- Wang, W.; Bao, J.; Zhou, W.; Chen, D.; Chen, D.; Yuan, L.; and Li, H. 2022b. Semantic image synthesis via diffusion models. *arXiv preprint arXiv:2207.00050*.
- Wang, W.; Bao, J.; Zhou, W.; Chen, D.; Chen, D.; Yuan, L.; and Li, H. 2025. Sindiffusion: Learning a diffusion model from a single natural image. *IEEE Transactions on Pattern Analysis and Machine Intelligence*.
- Wang, Z.; Bovik, A. C.; Sheikh, H. R.; and Simoncelli, E. P. 2004. Image quality assessment: from error visibility to structural similarity. *IEEE transactions on image processing*, 13(4): 600–612.
- Wang, Z.; Yang, Y.; Chen, Y.; Yuan, T.; Sermesant, M.; Delingette, H.; and Wu, O. 2024. Mutual information guided diffusion for zero-shot cross-modality medical image translation. *IEEE Transactions on Medical Imaging*.
- Wu, C. H.; and De la Torre, F. 2023. A latent space of stochastic diffusion models for zero-shot image editing and guidance. In *Proceedings of the IEEE/CVF International Conference on Computer Vision*, 7378–7387.
- Xia, B.; Zhang, Y.; Wang, S.; Wang, Y.; Wu, X.; Tian, Y.; Yang, W.; Timotfe, R.; and Van Gool, L. 2024a. Diffi2i: efficient diffusion model for image-to-image translation. *IEEE Transactions on Pattern Analysis and Machine Intelligence*.
- Xia, M.; Zhou, Y.; Yi, R.; Liu, Y.-J.; and Wang, W. 2024b. A diffusion model translator for efficient image-to-image translation. *IEEE Transactions on Pattern Analysis and Machine Intelligence*.
- Xia, Y.; Feng, S.; Zhao, J.; and Yuan, Z. 2024c. Robust Cross-modal Medical Image Translation via Diffusion Model and Knowledge Distillation. In *2024 International Joint Conference on Neural Networks (IJCNN)*, 1–8. IEEE.
- Xing, Z.; Yang, S.; Chen, S.; Ye, T.; Yang, Y.; Qin, J.; and Zhu, L. 2024. Cross-conditioned diffusion model for medical image to image translation. In *International Conference on Medical Image Computing and Computer-Assisted Intervention*, 201–211. Springer.
- Yang, B.; Gu, S.; Zhang, B.; Zhang, T.; Chen, X.; Sun, X.; Chen, D.; and Wen, F. 2023. Paint by example: Exemplar-based image editing with diffusion models. In *Proceedings of the IEEE/CVF Conference on Computer Vision and Pattern Recognition*, 18381–18391.
- Yi, Z.; Zhang, H.; Tan, P.; and Gong, M. 2017. Dualgan: Unsupervised dual learning for image-to-image translation. In *Proceedings of the IEEE international conference on computer vision*, 2849–2857.
- Yin, W.; Yu, Y.; Yin, H.; Kragic, D.; and Björkman, M. 2024. Scalable motion style transfer with constrained diffusion generation. In *Proceedings of the AAAI Conference on Artificial Intelligence*, volume 38, 10234–10242.
- Yu, J.; Zhang, X.; Xu, Y.; and Zhang, J. 2023. Cross: Diffusion model makes controllable, robust and secure image steganography. *Advances in neural information processing systems*, 36: 80730–80743.
- Zamir, S. W.; Arora, A.; Khan, S.; Hayat, M.; Khan, F. S.; and Yang, M.-H. 2022. Restormer: Efficient transformer for high-resolution image restoration. In *Proceedings of the IEEE/CVF conference on computer vision and pattern recognition*, 5728–5739.
- Zhang, B.; Zhu, X.; Zhang, X.; and Lei, Z. 2023a. Modeling spoof noise by de-spoofing diffusion and its application in face anti-spoofing. In *2023 IEEE International Joint Conference on Biometrics (IJCB)*, 1–10. IEEE.
- Zhang, J.; Rimchala, J.; Mouatadid, L.; Das, K.; and Kumar, S. 2024. DECDM: Document enhancement using cycle-consistent diffusion models. In *Proceedings of the IEEE/CVF Winter Conference on Applications of Computer Vision*, 8036–8045.
- Zhang, R.; Isola, P.; and Efros, A. A. 2016. Colorful image colorization. In *Computer Vision—ECCV 2016: 14th European Conference, Amsterdam, The Netherlands, October 11–14, 2016, Proceedings, Part III 14*, 649–666. Springer.
- Zhang, X.; Zhang, L.; Guo, H.; Zheng, H.; Sun, H.; Li, Y.; Li, R.; Luan, C.; and Tong, X. 2025. DCLTV: An Improved Dual-Condition Diffusion Model for Laser-Visible Image Translation. *Sensors*, 25(3): 697.
- Zhang, Z.; Han, L.; Ghosh, A.; Metaxas, D. N.; and Ren, J. 2023b. Sine: Single image editing with text-to-image diffusion models. In *Proceedings of the IEEE/CVF Conference on Computer Vision and Pattern Recognition*, 6027–6037.
- Zhao, M.; Bao, F.; Li, C.; and Zhu, J. 2022. Egsde: Unpaired image-to-image translation via energy-guided stochastic differential equations. *Advances in Neural Information Processing Systems*, 35: 3609–3623.
- Zheng, G.; Zhou, X.; Li, X.; Qi, Z.; Shan, Y.; and Li, X. 2023. Layoutdiffusion: Controllable diffusion model for layout-to-image generation. In *Proceedings of the IEEE/CVF Conference on Computer Vision and Pattern Recognition*, 22490–22499.
- Zhu, J.-Y.; Park, T.; Isola, P.; and Efros, A. A. 2017. Unpaired image-to-image translation using cycle-consistent adversarial networks. In *Proceedings of the IEEE international conference on computer vision*, 2223–2232.

# Appendix

## A. Additional references

The application of DMs in I2I translation has experienced significant advancements, primarily due to their ability to generate high-quality and diverse outputs. Ho et al. (Su et al. 2022) introduced DDPMs, which achieved training stability through adopting a simplified noise scheduling strategy, thereby establishing a robust foundation for future investigations in this field. The introduction of Stable Diffusion (Rombach et al. 2022) facilitated text-to-image generation by employing latent space compression and cross-attention mechanisms, making it a cornerstone for I2I translation. Subsequently, Saharia et al. developed Palette (Saharia et al. 2022a), a conditional diffusion framework that outperformed GANs in tasks such as colorization and image inpainting by utilizing source image conditioned iterative denoising. A brief overview of additional relevant research in this area follows:

**Unpaired I2I translation.** Unpaired I2I translation aims to learn cross-domain mappings without requiring paired data. The seminal work (Sasaki, Willcocks, and Breckon 2021) introduced DMs to unpaired settings via joint distribution modeling. Su et al. (Su et al. 2022) employed independently trained DMs with PF-ODEs for translation, while Zhao et al. (Zhao et al. 2022) used energy functions to preserve domain-invariant features. Other studies (Li et al. 2023a; Kim and Chung 2024; Kim et al. 2023) treated translation as a stochastic Brownian bridge. Prompt-free methods (Parmar et al. 2023) leveraged editing directions and cross-attention guidance, and Tu et al. (Tu, Wang, and Zhao 2024) improved diversity via diffusion adversarial networks and singular value decomposition (SVD)-based feature fusion. Luo et al. (Luo et al. 2024) further introduced a target-guided strategy for unpaired cross-modal medical image translation.

**I2I translation in different fields.** (1) Medical Imaging: Several technologies have been developed to preserve anatomical structures, including conditional adversarial diffusion (Xia et al. 2024b), contour-based representations (Chen), and frequency band separation (Li et al. 2023b). Graf et al. (Graf et al. 2023) employed DMs to translate Magnetic Resonance Imaging into Computed Tomography images for automated spine segmentation. Wang et al. (Wang et al. 2024) facilitated cross-modal alignment through interactive information guidance. Xing et al. (Xing et al. 2024) introduced cross-conditional DMs that leveraged target image distributions to enhance both the quality and efficiency of medical image translation. Patil et al. (Patil et al. 2025) proposed a unified framework for single-source to multi-target translation in multi-modal medical imaging. (2) Remote Sensing and Sensors: Brownian bridge processes have been applied to Synthetic Aperture Radar (SAR)-to-optical image translation (Guo et al. 2024; Shi et al. 2024a) and laser-to-visible light conversion (Zhang et al. 2025). Vinholi et al. (Vinholi et al. 2024) enhanced the spatial resolution of optical images using DMs while ensuring radiometric consistency. Bai et al. sequentially incorporated SAR image conditioning (Bai, Pu, and Xu 2023) and color information (Bai and Xu 2024) into DMs to improve

translation fidelity. (3) Video Processing: Ceylan et al. (Ceylan, Huang, and Mitra 2023) preserved temporal coherence by editing anchor frames and integrating self-attention features with depth conditioning.

**Structure preservation and Geometric alignment.** Ensuring geometric consistency is crucial in image translation. RePaint (Lugmayr et al. 2022) preserved structural integrity during inpainting by iteratively sampling masked regions using unconditional DDPM priors. Lin et al. (Lin et al. 2023) maintained original content shapes in zero-shot I2I by leveraging rich cross-attention maps. Li et al. (Li and Ma 2023) mitigated structural distortion by integrating domain-independent geometric features with target appearances. Zheng et al. (Zheng et al. 2023) enhanced multi-object generation control through layout fusion modules and object-aware attention mechanisms. Han et al. (Han et al. 2024) combined DMs with GPT architectures, enabling interpretable visual programming control and offering a novel approach to guiding image translation while preserving geometric fidelity. Finally, the study in (Lin et al. 2024) further improved geometric consistency by aligning text prompts and latent codes to mirror source and target images.

**Multi-modal and cross-modal generation.** Liu et al. (Liu and Chang 2024) leveraged style reference images and segmentation masks for conditional generation. Additionally, Gao et al. (Gao et al. 2024) introduced frequency band separation to regulate text-guided translation processes. Sun et al. (Sun et al. 2023) decomposed score functions on manifolds to optimize entangled distributions. Kim et al. (Kim and Park 2024) focused on translating 3D medical images from single- to multi-modal outputs. CRoSS (Yu et al. 2023) employed DDIM inversion for reversible steganography. Finally, Wang et al. (Wang et al. 2025) modeled patch distributions from single natural images to facilitate diverse image generation.

Beyond these categories, recent explorations include CRoSS (Yu et al. 2023) for reversible steganography and Robust Cross-Moda (Xia et al. 2024c), which improves adversarial robustness through knowledge distillation.

## B. Assumptions

We adopt the theoretical assumptions from (Song et al. 2021; Kwon, Fan, and Lee 2022). Notably, we present only the assumptions relevant to the source domain  $DM^A$ . The corresponding assumptions for the target domain  $DM^B$  can be obtained analogously by replacing  $A$  with  $B$ .

**Assumption 5.** *Both the drift term  $f^A(x^A, t)$  and score network  $S_\theta^A(x^A, t)$  are Lipschitz continuous with respect to variable  $x^A$ , namely, there exist two scale continuous functions  $L_f^A(t), L_{S_\theta}^A(t) : [0, T] \rightarrow \mathbb{R}_{>0}$ , holding  $\|f^A(x^A, t) - f^A(y^A, t)\|_2 \leq L_f^A(t) \|x^A - y^A\|_2$  and  $\|S_\theta^A(x^A, t) - S_\theta^A(y^A, t)\|_2 \leq L_{S_\theta}^A(t) \|x^A - y^A\|_2$  for any  $x^A, y^A \in \mathbb{R}^n$ , respectively. In addition, there exists constant  $C_g > 0$  for all  $t \in [0, T]$  such that  $\frac{1}{C_g} < g^A(t) < C_g$ .*

**Assumption 6.** *There exists constant  $C_p > 0$  that satisfies  $\{\|S_\theta^A(x^A, t)\|_2, \|\nabla \log p_t^A(x^A)\|_2\} \leq C_p(1 + \|x^A\|_2)$  for any  $x^A \in \mathbb{R}^n$  and  $t \in [0, T]$ .*

**Assumption 7.** The score network  $\mathbf{S}_\theta^A(\mathbf{x}^A, t)$  and probability density  $p_t^A(\mathbf{x}^A)$  satisfy conditions  $\{\int_0^T \mathbb{E}_{p_t^A} [\|\mathbf{S}_\theta^A(\mathbf{x}^A, t)\|_2^2] dt, \int_0^T \mathbb{E}_{p_t^A} [\|\nabla \log p_t^A(\mathbf{x}^A)\|_2^2] dt\} < +\infty$ .

**Assumption 8.** There exists constant  $C_e > 0$  for all  $t \in [0, T]$  such that  $\{p_t^A(\mathbf{x}^A), q_t^A(\mathbf{x}^A)\} = \mathcal{O}(\exp(-\|\mathbf{x}^A\|_2^{C_e}))$ .

**Assumption 9.** We assume that  $DM^A$  is precisely trained, i.e.,  $\mathbf{S}_\theta^A(\mathbf{x}^A, t) \equiv \nabla \log p_t^A(\mathbf{x}^A)$  for all  $t \in [0, T]$  and  $\mathbf{x}^A \in \mathbb{R}^n$ .

### C. Geometric variational principle of OT map

Supposing  $\mathcal{Y}^B = \{\mathbf{y}_i^B\}_{i \in \mathcal{I}} \stackrel{i.i.d.}{\sim} p_T^B$  is the set of discrete points, here we introduce geometric variational methods (Gu et al. 2013) for calculating the OT map from  $p_T^A$  to  $\frac{1}{|\mathcal{I}|} \sum_{i \in \mathcal{I}} \delta(\mathbf{y}^B - \mathbf{y}_i^B)$ . The dual of Monge problem (8) in main text is

$$\begin{aligned} \max_{\psi} E(\psi) &= \int_{\mathbb{R}^n} \psi^c(\mathbf{x}^B) p_T^A(\mathbf{x}^B) d\mathbf{x}^B + \frac{1}{|\mathcal{I}|} \sum_{i \in \mathcal{I}} \psi_i \\ &= \sum_{i \in \mathcal{I}} \int_{W_i(\psi)} (\langle \mathbf{y}_i^B, \mathbf{x}^A \rangle - \psi_i) d\mathbf{x}^A + \frac{1}{|\mathcal{I}|} \sum_{i \in \mathcal{I}} \psi_i, \end{aligned} \quad (9)$$

where  $\psi_i = \psi(\mathbf{y}_i^B)$ ,  $\psi^c(\mathbf{x}^A) = \min_i \frac{1}{2} \|\mathbf{x}^A - \mathbf{y}_i^B\|_2^2 - \psi_i$  and  $W_i(\psi) = \{\mathbf{x}^A \in \mathbb{R}^n | \langle \mathbf{y}_i^B - \mathbf{y}_j^B, \mathbf{x}^A \rangle \geq \psi_i - \psi_j, \forall j \in \mathcal{I}\}$  implies nearest power Voronoi diagram. Each target point  $\mathbf{y}_i^B$  corresponds to a support plane  $\pi_i = \langle \mathbf{x}^A, \mathbf{y}_i^B \rangle + \psi_i - \frac{1}{2} \|\mathbf{y}_i^B\|_2^2$ , therefore the Brenier potential energy can be constructed as  $u_{\mathbf{h}}(\mathbf{x}^A) = \max_i \langle \mathbf{x}^A, \mathbf{y}_i^B \rangle + h_i$ , here  $h_i = \psi_i - \frac{1}{2} \|\mathbf{y}_i^B\|_2^2$ . We optimize the energy function  $E(\psi)$  in (9) through the Monte Carlo algorithm (An et al. 2020) to obtain Brenier potential  $u_{\mathbf{h}}$ . Referring to this geometric property, the image of  $\nabla u_{\mathbf{h}}$  falls precisely within the data set  $\mathcal{Y}$ , namely  $\nabla u_{\mathbf{h}}(\mathbf{x}^A) \in \mathcal{Y}$  for any  $\mathbf{x}^A \sim p_T^A$ . We denote the OT map from  $p_T^A$  to  $p_T^B$  as  $u_T^{A \rightarrow B}$ , so there is  $u_{\mathbf{h}} \rightarrow u_T^{A \rightarrow B}$  when  $|\mathcal{I}| \rightarrow +\infty$ .

### D. Proofs

In this section, we give a detailed derivation of the main theories proposed in this paper.

#### D.1 Proof of Theorem 1

*Proof.* It can be directly proved based on the contraction property of Wasserstein distance (Carrillo, McCann, and Villani 2006)

$$\mathcal{W}_2(p_T^B, q_T^B) \leq \exp\left(-\frac{1}{2} \int_0^T L_f^B(t) dt\right) \mathcal{W}_2(p_0^B, q_0^B) \quad (10)$$

and Theorem 1 in (Kwon, Fan, and Lee 2022). The scale function  $L_f^B(t)$  in (10) satisfies  $\lim_{T \rightarrow \infty} \int_0^T L_f^B(t) dt = \infty$ .  $\square$

#### D.2 Proof of Theorem 2

*Proof.* On the basis of Theorem 1 in (Kwon, Fan, and Lee 2022), we have

$$\begin{aligned} &\mathcal{W}_2(p_0^B, q_0^B) \\ &\leq \int_0^T \phi^B(t)^{\frac{1}{2}} \mathbb{E}_{p_t^B} [\|\nabla \log p_t^B(\mathbf{x}^B) - \mathbf{S}_\theta^B(\mathbf{x}^B, t)\|_2^2]^{\frac{1}{2}} dt \\ &\quad + I(T) \mathcal{W}_2(p_T^B, q_T^B) \\ &\leq \sqrt{2T} \mathcal{J}_{SM}^B(\theta^B, \phi^B, T)^{\frac{1}{2}} + I(T) \mathcal{W}_2(p_T^B, q_T^B) \\ &= \sqrt{2T} (\mathcal{J}_{SM}^B)^{\frac{1}{2}} + I(T) \mathcal{W}_2(\nabla u_T^{A \rightarrow B}(p_T^A), \nabla u_{\mathbf{h}}(p_T^A)), \end{aligned} \quad (11)$$

where  $I^B(T) = \exp\left(\int_0^T (L_f^B(t) + \frac{g^B(t)^2}{2} L_{\mathbf{S}_\theta^B}^B(t)) dt\right)$ ,  $\star$  is derived from the Cauchy-Schwartz inequality and  $\phi^B = (g^B)^4 (I^B)^2$ . Referring to Proposition 2.1 of (Mérigot, Delalande, and Chazal 2020) and Theorem 22 in (Chazal et al. 2017), we concern with the last term of the above inequality in the following form

$$\begin{aligned} &\mathcal{W}_2(\nabla u_T^{A \rightarrow B}(p_T^A), \nabla u_{\mathbf{h}}(p_T^A)) \\ &\leq \|\nabla u_T^{A \rightarrow B} - \nabla u_{\mathbf{h}}\|_{L_2(p_T^A)} \\ &= \left( \int_{\mathbb{R}^n} \|\nabla u_T^{A \rightarrow B}(\mathbf{x}^A) - \nabla u_{\mathbf{h}}(\mathbf{x}^A)\|_2^2 p_T(\mathbf{x}^A) d\mathbf{x}^A \right)^{\frac{1}{2}} \\ &\leq \left( \int_{\mathbb{R}^n} \|\nabla u_T^{A \rightarrow B}(\mathbf{x}^A) - \nabla u_{\mathbf{h}}(\mathbf{x}^A)\|_2^2 d\mathbf{x}^A \right)^{\frac{1}{2}} \\ &\leq 2K_1 \|u_T^{A \rightarrow B} - u_{\mathbf{h}}\|_{\infty}^{\frac{1}{2}} (\|\nabla u_T^{A \rightarrow B}\|_{\infty}^{\frac{1}{2}} + \|\nabla u_{\mathbf{h}}\|_{\infty}^{\frac{1}{2}}) \\ &\leq 4K_1 K_2 \|u_T^{A \rightarrow B} - u_{\mathbf{h}}\|_{\infty}^{\frac{1}{2}}, \end{aligned} \quad (12)$$

where  $K_1$  and  $K_2$  are constants, respectively. Then we can prove the below formula

$$\mathcal{W}_2(p_0^B, q_0^B) \leq \sqrt{2T} (\mathcal{J}_{SM}^B)^{\frac{1}{2}} + KI(T) \|u_T^{A \rightarrow B} - u_{\mathbf{h}}\|_{\infty}^{\frac{1}{2}} \quad (13)$$

by taking  $K = 4K_1 K_2$  and applying (12) to (11).  $\square$

#### D.3 Proof of Theorem 3

*Proof.* All diffusion process can be described by a deterministic ODE with matching marginal distributions, known as the PF-ODE (Song et al. 2020), which uniquely encodes the data. For the forward SDE (1) in main text, the corresponding PF-ODE is shown as (3) in main text. In the reverse process, we replace  $\nabla \log p_t^{A/B}(\mathbf{x}^{A/B})$  with the trained, parameterized score network  $\mathbf{S}_\theta^{A/B}(\mathbf{x}^{A/B}, t)$  to obtain an approximate PF-ODE

$$d\mathbf{x}^{A/B} = (\mathbf{f}^{A/B}(\mathbf{x}^{A/B}, t) - \frac{g^{A/B}(t)^2}{2} \mathbf{S}_\theta^{A/B}(\mathbf{x}^{A/B}, t)) dt. \quad (14)$$

When  $\eta = 0$ , the mapping from  $\mathbf{x}_{t_0}^{A/B}$  to  $\mathbf{x}_{t_1}^{A/B}$  then can be formulated as

$$\begin{aligned} & \text{Solver}_\eta(\mathbf{x}_{t_0}^{A/B}, \mathbf{S}_\theta^{A/B}, t_0, t_1) \\ &= \mathbf{x}_0^{A/B} + \int_{t_0}^{t_1} (\mathbf{f}^{A/B}(\mathbf{x}_t^{A/B}, t) \\ & \quad - \frac{g^{A/B}(t)^2}{2} \mathbf{S}_\theta^{A/B}(\mathbf{x}_t^{A/B}, t)) dt \end{aligned} \quad (15)$$

Under the premise that Assumption 5 is satisfied and the discretization error is ignored,  $\text{Solver}_\eta$  completely follows PF-ODE (14). Further, when the calculation error of OT is not taken into account, then we have  $M_{ot,T}^{A \rightarrow B} \circ M_{ot,T}^{B \rightarrow A}(\mathbf{x}^{A/B}) = \mathbf{x}^{A/B}$  for any  $\mathbf{x}^{A/B} \in \mathbb{R}^n$ . Based on the above analysis, OT-ALD satisfies the sample-level cycle consistency.  $\square$

#### D.4 Proof of Theorem 4

*Proof.* Even if noise is introduced, namely,  $\eta > 0$ , the marginal distribution  $p_t^{A/B}$  always satisfies FPE (2) in main text. Under the premise that Assumption 5 is satisfied, and the discretization error and calculation error of OT are ignored, we have  $q_T^B = M_{ot,T}^{A \rightarrow B}(p_T^A) = p_T^B$  and  $q_T^A = M_{ot,T}^{B \rightarrow A}(p_T^B) = p_T^A$ , which ensures that the forward FPE and approximate reverse FPE are equivalent (Kwon, Fan, and Lee 2022). Therefore,  $q_0^B = p_0^B$ , and further we have  $p_0^A = p_0^A$  is satisfied. Based on the above analysis, OT-ALD satisfies the distributional-level cycle consistency.  $\square$

## E. More experimental details and visual results

### E.1 More experimental details Hardware and Setup.

The experiments were conducted on an NVIDIA RTX 4090 cluster, utilizing CUDA 12.1 acceleration and implemented using the PyTorch framework.

**Codebase.** Our model is implemented based on the official GitHub repository from OpenAI (<https://github.com/openai/guided-diffusion>). All baseline models are reproduced using their respective official implementations: EGSDE is implemented using <https://github.com/ML-GSAI/EGSDE> with  $T = 1000$ ; CUT and CycleGAN use <https://github.com/taesungp/contrastive-unpaired-translation>; ILVR is based on [https://github.com/jychoi118/ilvr\\_adm](https://github.com/jychoi118/ilvr_adm) with  $T = 1000$ ; SDEdit uses <https://github.com/ermongroup/SDEdit> with  $T = 500$  and  $K = 2$  repetitions; and DDIB is implemented with <https://github.com/suxuann/ddib>. All hyperparameters follow the settings reported in the original papers.

**Implementation Parameters.** The OT-ALD introduced in this study is compared strictly in the same DDIM (Song, Meng, and Ermon 2021) backbone, employing a linear noisy schedule defined by the parameters ( $\beta_1 = 1 \times 10^{-4}$ ,  $\beta_T = 0.02$ ,  $T = 1000$ ) for the AFHQ, CelebA-HQ and summer2winter dataset. More detailed hyperparameters are shown in Tab. 4. To construct the OT-ALD with truncation parameter  $T_{trun}$ , the initial values for  $\beta_1, \beta_2, \dots, \beta_T$  must first be established, followed by the cessation of the diffusion process at the  $T_{trun}$ -th step. To solve the Brenier potential energy  $u_h$  as delineated in (9) (main text), we employ

the geometric variational principle, as referenced in Section and (An et al. 2020). The number of Monte Carlo samples is established at  $N_{mc} = 10 \times |\mathcal{I}|$ . The learning rates for the datasets AFHQ, CelebA-HQ and summer2winter are set to  $lr = 1 \times 10^{-5}$ ,  $lr = 1 \times 10^{-5}$ , and  $lr = 2 \times 10^{-4}$ , respectively. To enhance convergence, we double the number of samples  $N_{mc}$  and reduce the learning rate  $lr$  by a factor of 0.8 if the energy function  $E(\mathbf{h})$  in (10) (main text) does not show a decrease over 50 iterations. Furthermore, a termination threshold  $\tau$  is set to  $8 \times 10^{-4}$ . The optimization procedure for  $\mathbf{h}$  will cease when  $E(\mathbf{h}) < \tau$  or when the total number of iterations surpasses 10000.

**E.2 More visual results** See Figs. 8-10.

Table 4: Optimization hyperparameters of OT-ALD on AFHQ, CelebA-HQ and summer2winter.

Hyperparameters	AFHQ-Cat ( $512 \times 512$ )	AFHQ-Dog ( $512 \times 512$ )	AFHQ-Wild ( $512 \times 512$ )
Noisy schedule	$\beta_1 = 1 \times 10^{-4}, \beta_T = 0.02$	$\beta_1 = 1 \times 10^{-4}, \beta_T = 0.02$	$\beta_1 = 1 \times 10^{-4}, \beta_T = 0.02$
$T$	1000	1000	1000
Number of residual blocks	3	3	3
Model channels	128	128	128
Channel multiple	(0.5, 1, 1, 2, 2, 4, 4)	(0.5, 1, 1, 2, 2, 4, 4)	(0.5, 1, 1, 2, 2, 4, 4)
Initial learning rate	$1 \times 10^{-4}$	$1 \times 10^{-4}$	$1 \times 10^{-4}$
Dropout	0.0	0.0	0.0
Adam optimizer $\beta_1^A$	0.5	0.5	0.5
Adam optimizer $\beta_2^A$	0.9	0.9	0.9
EMA	0.9999	0.9999	0.9999
Batch size	35	35	35
Number of training steps	3850000	3640000	3980000
Number of GPUs	1×RTX 4090 GPU	1×RTX 4090 GPU	1×RTX 4090 GPU
Hyperparameters	CelebA-HQ-Male ( $512 \times 512$ )	CelebA-HQ-Female ( $512 \times 512$ )	
Noisy schedule	$\beta_1 = 1 \times 10^{-4}, \beta_T = 0.02$	$\beta_1 = 1 \times 10^{-4}, \beta_T = 0.02$	
$T$	1000	1000	
Number of residual blocks	3	3	
Model channels	128	128	
Channel multiple	(0.5, 1, 1, 2, 2, 4, 4)	(0.5, 1, 1, 2, 2, 4, 4)	
Initial learning rate	$1 \times 10^{-4}$	$1 \times 10^{-4}$	
Dropout	0.0	0.0	
Adam optimizer $\beta_1^A$	0.5	0.5	
Adam optimizer $\beta_2^A$	0.9	0.9	
EMA	0.9999	0.9999	
Batch size	35	35	
Number of training steps	3820000	3770000	
Number of GPUs	1×RTX 4090 GPU	1×RTX 4090 GPU	
Hyperparameters	summer2winter-Summer ( $256 \times 256$ )	summer2winter-Summer ( $256 \times 256$ )	
Noisy schedule	$\beta_1 = 1 \times 10^{-4}, \beta_T = 0.02$	$\beta_1 = 1 \times 10^{-4}, \beta_T = 0.02$	
$T$	1000	1000	
Number of residual blocks	3	3	
Model channels	128	128	
Channel multiple	(1, 1, 2, 2, 4, 4)	(1, 1, 2, 2, 4, 4)	
Initial learning rate	$1 \times 10^{-4}$	$1 \times 10^{-4}$	
Dropout	0.0	0.0	
Adam optimizer $\beta_1^A$	0.5	0.5	
Adam optimizer $\beta_2^A$	0.9	0.9	
EMA	0.9999	0.9999	
Batch size	35	35	
Number of training steps	4370000	4460000	
Number of GPUs	1×RTX 4090 GPU	1×RTX 4090 GPU	

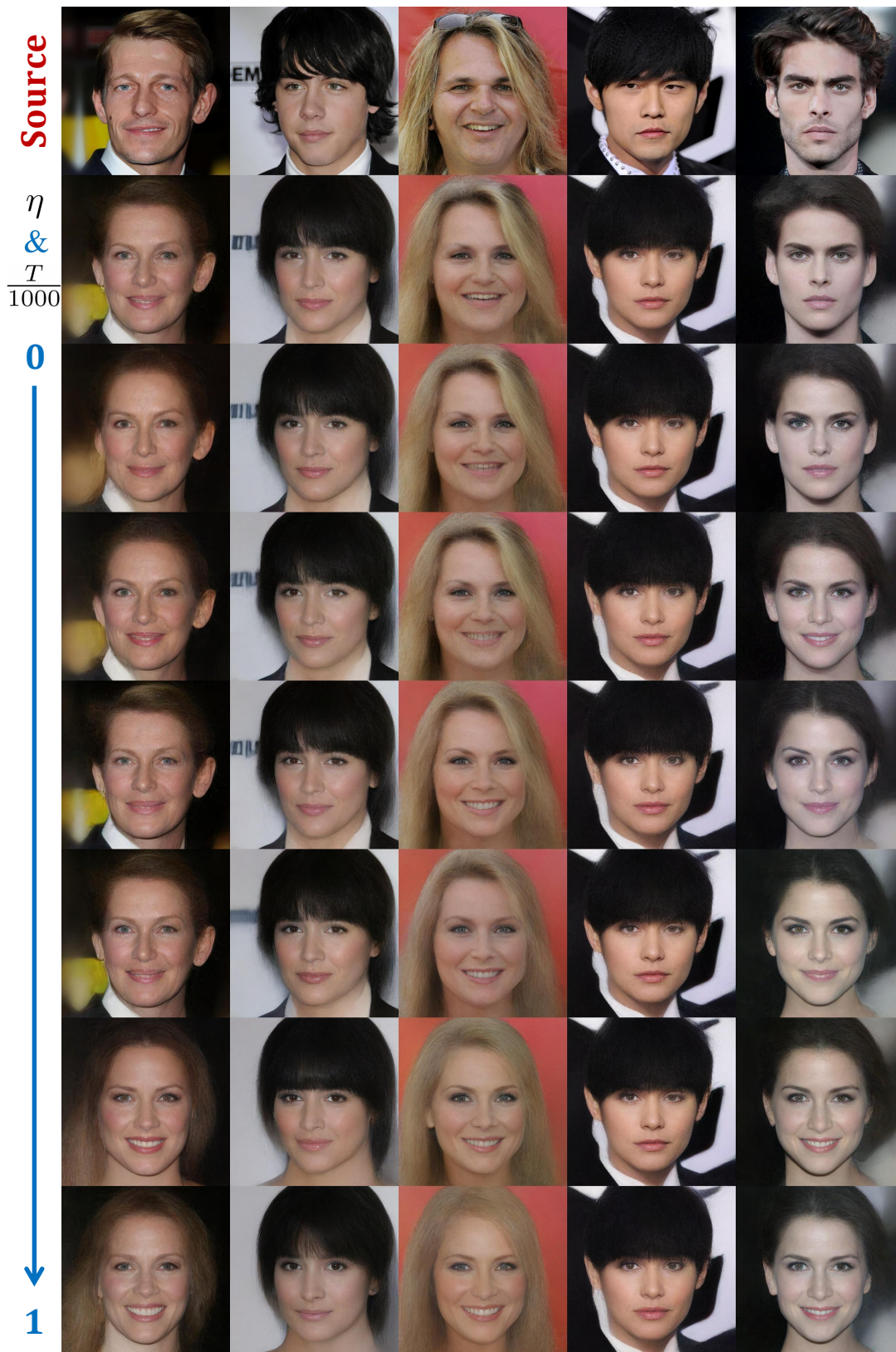


Fig 8: Visualization of the translation results of OT-ALD with different  $\eta$  and  $T$  on Mela→Female task.

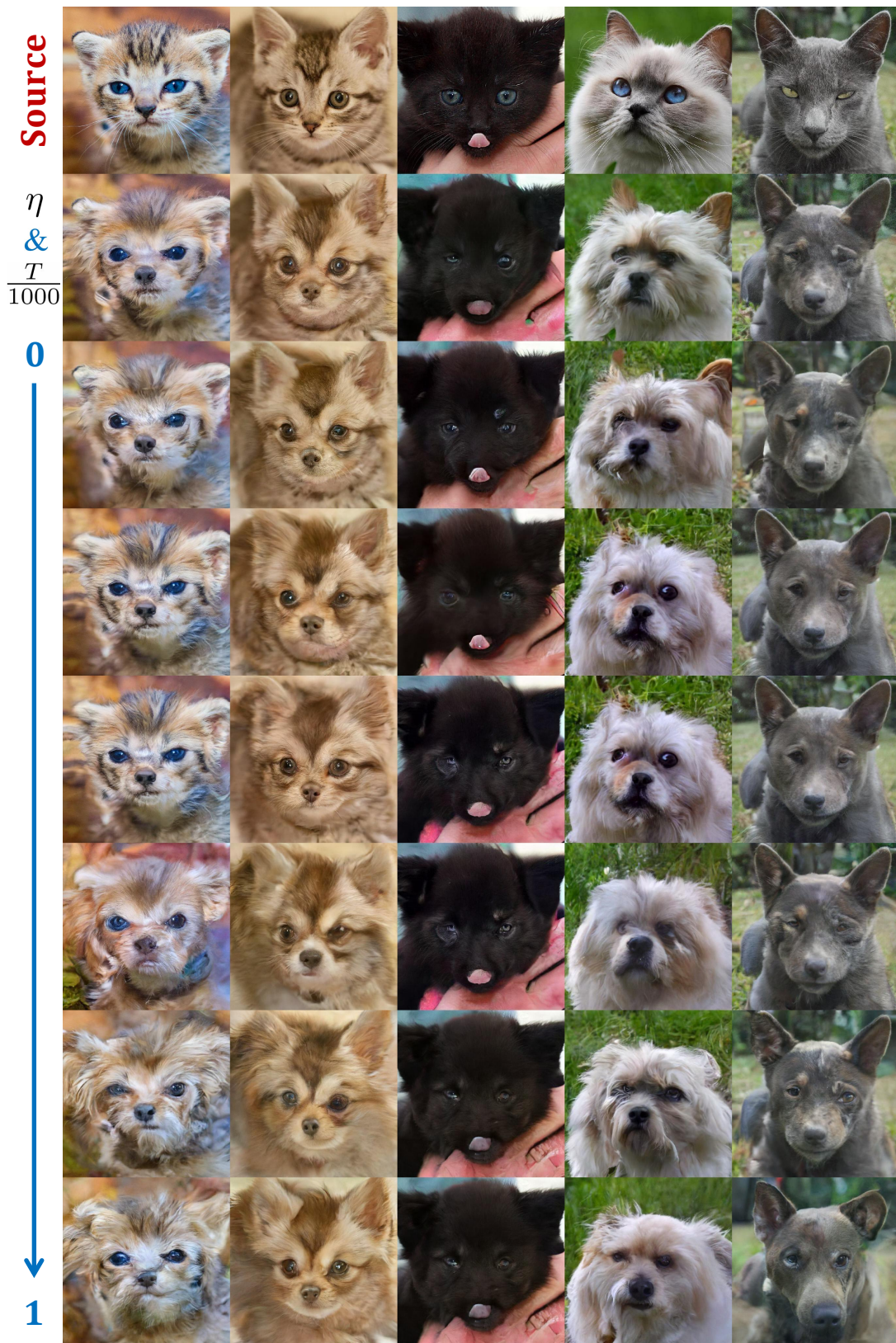


Fig 9: Visualization of the translation results of OT-ALD with different  $\eta$  and  $T$  on Cat→Dog task.

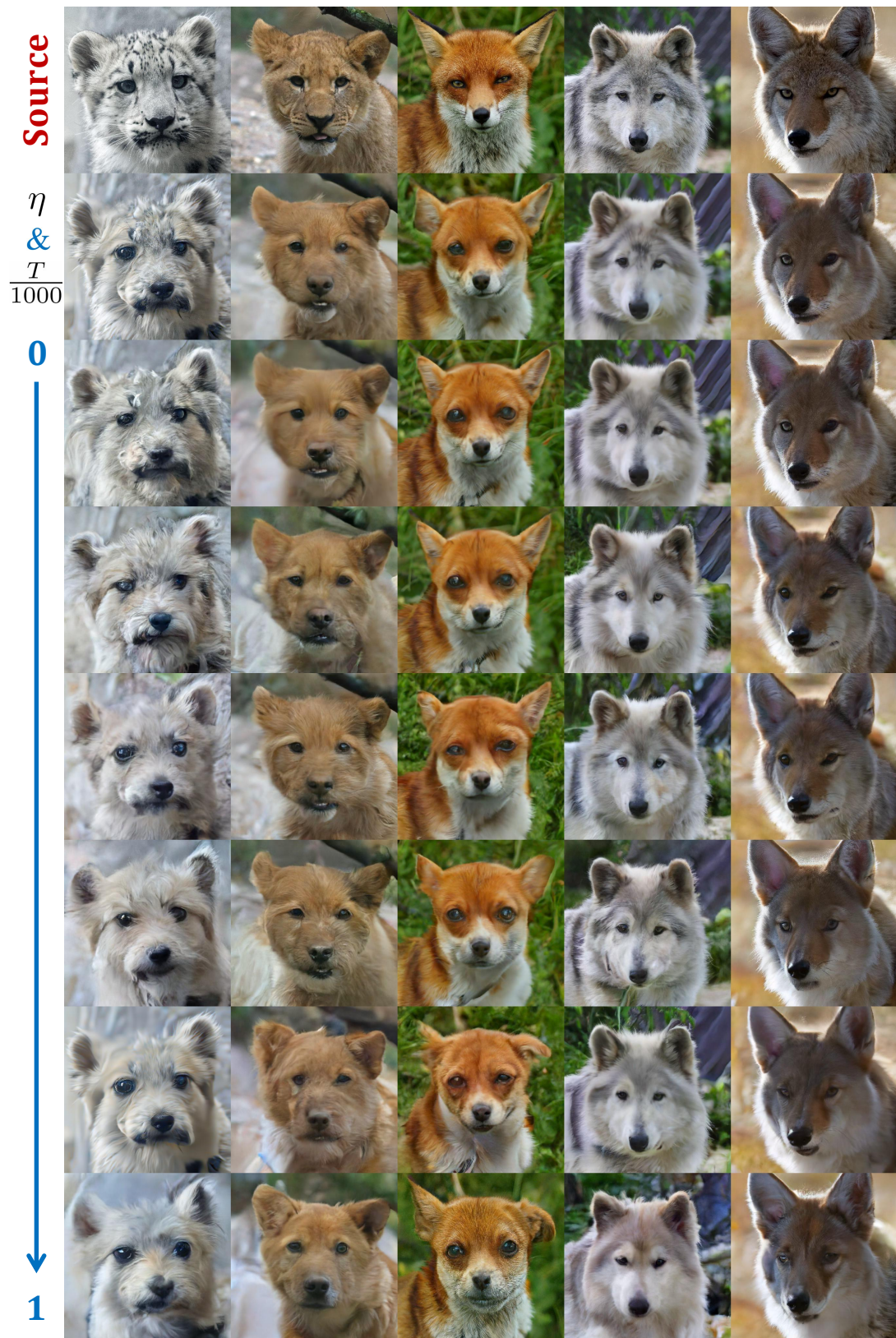


Fig 10: Visualization of the translation results of OT-ALD with different  $\eta$  and  $T$  on Wild→Dog task.